The Evolution of Lake-Effect Convection during Landfall and Orographic Uplift as Observed by Profiling Radars

JUSTIN R. MINDER AND THEODORE W. LETCHER

University at Albany, State University of New York, Albany, New York

LEAH S. CAMPBELL, PETER G. VEALS, AND W. JAMES STEENBURGH

University of Utah, Salt Lake City, Utah

(Manuscript received 27 March 2015, in final form 15 July 2015)

ABSTRACT

A pronounced snowfall maximum occurs about 30 km downwind of Lake Ontario over the 600-m-high Tug Hill Plateau (hereafter Tug Hill), a region where lake-effect convection is affected by mesoscale forcing associated with landfall and orographic uplift. Profiling radar data from the Ontario Winter Lake-effect Systems field campaign are used to characterize the inland evolution of lake-effect convection that produces the Tug Hill snowfall maximum. Four K-band profiling Micro Rain Radars (MRRs) were aligned in a transect from the Ontario coast onto Tug Hill. Additional observations were provided by an X-band profiling radar (XPR). Analysis is presented of a major lake-effect storm that produced 6.4-cm liquid precipitation equivalent (LPE) snowfall over Tug Hill. This event exhibited strong inland enhancement, with LPE increasing by a factor of 1.9 over 15-km horizontal distance. MRR profiles reveal that this enhancement was not due to increases in the depth or intensity of lake-effect convection. With increasing inland distance, echoes transitioned from a convective toward a stratiform morphology, becoming less intense, more uniform, more frequent, and less turbulent. An inland increase in echo frequency (possibly orographically forced) contributes somewhat to snowfall enhancement. The XPR observations reproduce the basic vertical structure seen by the MRRs while also revealing a suppression of snowfall below 600 m AGL upwind of Tug Hill, possibly associated with subcloud sublimation or hydrometeor advection. Statistics from 29 events demonstrate that the above-described inland evolution of convection is common for lake-effect storms east of Lake Ontario.

1. Introduction and background

The region east of Lake Ontario (Fig. 1a) receives some of the largest seasonal snowfall totals in eastern North America. Annual average snowfall exceeds 450 cm (e.g., Eichenlaub and Hodler 1979; Burt 2007; Hartnett et al. 2014; Veals and Steenburgh 2015). Much of this snowfall is produced by lake-effect storms. These storms can produce snowfall rates that are among the most intense in the world, including 30.5 cm in 1 h at Copenhagen, New York, and 129.5 cm in 16 h at Bennett's Bridge, New York (Burt 2007).

Annual average (and frequently storm total) snowfall in this region has a distinct maximum over the 600-m-high Tug Hill Plateau (hereafter Tug Hill; Fig. 1) 20–30 km east of Lake Ontario (Eichenlaub and Hodler 1979; Reinking et al. 1993; Burt 2007; Hartnett et al. 2014; Veals and Steenburgh 2015). This study uses observations from the Ontario Winter Lake-effect Systems (OWLeS) field campaign to better understand how the inland evolution of lake-effect clouds produces the Tug Hill snowfall maximum.

a. *Lake-effect snow: Environmental controls and mesoscale morphologies*

Lake-effect snow is produced when cold air is advected over a relatively warm lake surface. If the lake–air temperature difference is sufficient, turbulent sensible and latent heat fluxes moisten and destabilize the boundary layer, leading to the formation of shallow, but often intense, convective clouds and snowfall. Lake-effect

Corresponding author address: Justin R. Minder, Department of Atmospheric and Environmental Sciences, University at Albany, State University of New York, 1400 Washington Avenue, Albany, NY 12222.
E-mail: jminder@albany.edu

DOI: 10.1175/MWR-D-15-0117.1

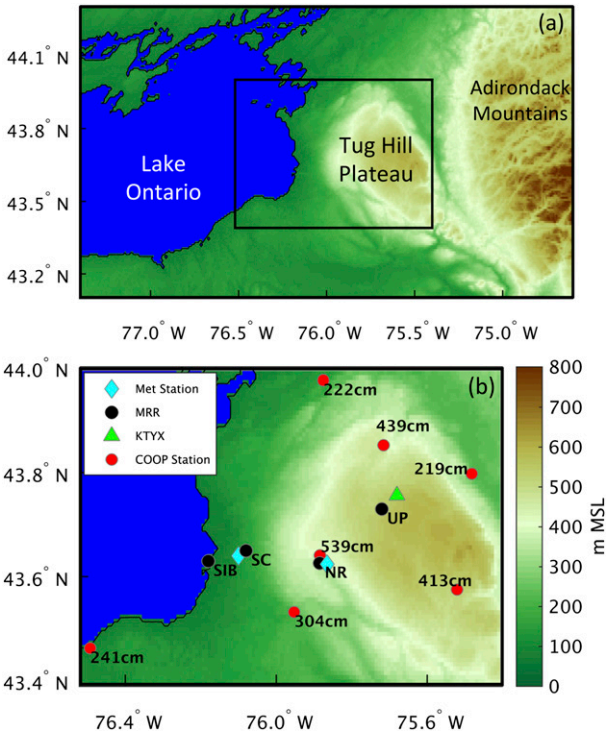

FIG. 1. Overview of the study area, showing (a) major geographic features and (b) measurement locations. Values in (b) indicate 13-yr annual average snowfall on days with lake-effect snow from COOP stations (from Veals and Steenburgh 2015). Terrain elevation is color shaded in both (a) and (b).

convection exhibits multiple modes of mesoscale organization, including widespread cellular convection, widespread wind-parallel linear roll circulations, localized wind-parallel bands, and localized mesoscale vortices (Hjelmfelt 1990; Niziol et al. 1995; Kristovich and Steve 1995). The crucial environmental factors determining the mode of organization include the lake-induced convective available potential energy (CAPE), the lake–land temperature difference, the height of the boundary layer capping inversion, the low-level wind speed and direction, the wind-relative geometry of the lake, and the geometry of nearby topography (e.g., Hjelmfelt 1990; Niziol et al. 1995; Onton and Steenburgh 2001; Laird et al. 2003a,b; Laird and Kristovich 2004; Alcott and Steenburgh 2013).

The most intense lake-effect snowfall usually occurs when the prevailing winds are oriented along the long axis of an elongated lake. In this case, land-breeze circulations can organize convection into a single wind-parallel band of strong horizontal convergence and intense snowfall (Peace and Sykes 1966; Passarelli and Braham 1981; Hjelmfelt and Braham 1983; Hjelmfelt 1990; Reinking et al. 1993; Niziol et al. 1995; Steiger et al. 2013). We refer to these as long-lake-axis-parallel (LLAP) bands, following Steiger et al. (2013).[1] LLAP bands generally have a horizontal width of 5–50 km and a length of 50–200 km (Peace and Sykes 1966; Reinking et al. 1993; Niziol et al. 1995; Steiger et al. 2013). The line of horizontal convergence and vertical motion associated with LLAP bands is often less than 5 km wide, much narrower than the band of snowfall (Peace and Sykes 1966; Reinking et al. 1993; Steiger et al. 2013).

Although the dynamical cause of lake-effect snow is convective instability, lake-effect cloud morphologies can be stratiform or convective in character. Broadly, clouds classified as convective have updrafts strong enough to loft ice and snow particles (exceeding $\sim 1\,\mathrm{m\,s^{-1}}$), high spatial and temporal variability, and supercooled water droplets that facilitate hydrometeor growth by collection. In contrast, stratiform clouds have weaker updrafts, reduced horizontal and temporal variability, and a dominance of depositional growth of ice crystals [see Houze (1997, 2014, chapter 6)]. Lake-effect convection often contains convective regions of localized strong horizontal convergence and high reflectivity adjacent to stratiform regions with weaker convergence and more homogenous weaker echoes (Reinking et al. 1993; Steiger et al. 2013). Presumably, these stratiform regions are generated similarly to the deep convective case: ice crystals initiated in strong convective updrafts are spread laterally and slowly precipitate to the surface, growing by diffusion in a surrounding region of weak ascent (Biggerstaff and Houze 1991; Yuter and Houze 1995b; Houze 1997).

b. *Snowfall characteristics east of Lake Ontario*

The region immediately east of Lake Ontario lies downwind of the long axis of the lake under prevailing westerly flow (Fig. 1), an ideal location for frequent and intense lake-effect snowfall. On average, over 900 h of lake-effect snow occurs per cold season in this region (Veals and Steenburgh 2015). The highest frequency of occurrence is in December–February (Kristovich and Steve 1995; Veals and Steenburgh 2015), when lake–air temperature differences are large and temperatures are cold enough for snow to occur (Holroyd 1971; Niziol et al. 1995).

Numerous studies indicate a local maximum in lake-effect snowfall over Tug Hill, centered on its western slopes and upper elevations (Eichenlaub and Hodler

[1] LLAP bands are also sometimes referred to as midlake or shoreline bands, depending on the location of the convection relative to the lake shore.

1979; Reinking et al. 1993; Burt 2007; Hartnett et al. 2014; Veals and Steenburgh 2015). Recently, Veals and Steenburgh (2015) analyzed 13 cold seasons of daily COOP surface observations and radar imagery (from the KTYX WSR-88D; Fig. 1b) over the Tug Hill region. They found a maximum in annual mean snowfall on days with lake-effect snow of 539 cm in north Redfield (NR), more than double the values just north of Tug Hill and on the Lake Ontario coast to the southwest (Fig. 1b). Additionally, they found a local maximum in the frequency of radar echoes exceeding given equivalent radar reflectivity, Z_e, thresholds (10 and 30 dBZ_e) over NR and central Tug Hill. During lake-effect periods, "broad coverage" was the most common morphology (present 84% of the time), followed by LLAP (24%).[2]

The physical mechanisms responsible for this localized snowfall maximum over Tug Hill have not been clearly discerned. All else being equal, one might expect a monotonic decrease in snowfall downwind of the lake, since the loss of surface heat and moisture fluxes should cause convection to weaken as it moves inland. Several authors have suggested that the topography of Tug Hill plays an important role in locally enhancing lake-effect snowfall (Reinking et al. 1993; Niziol et al. 1995; Veals and Steenburgh 2015). Modeling studies have diagnosed orographic enhancement of lake-effect snowfall over the modest topography (200–500-m relief) adjacent to Lakes Michigan and Erie and the much taller topography of the Wasatch Mountains (1–2-km relief) adjacent to the Great Salt Lake (Lavoie 1972; Hjelmfelt 1992; Onton and Steenburgh 2001; Alcott and Steenburgh 2013). Other simulations indicate that the mountains of Japan enhance snowfall from convective sea-effect clouds generated over the Sea of Japan (Murakami et al. 1994; Saito et al. 1996). Our analysis of snowfall over Tug Hill contrasts with previous studies of orographic effects on lake-effect snow in that it relies on detailed field observations (in contrast with the above-mentioned numerical studies) and focuses on a location with modest topography (in contrast to the mountains of Japan and Utah) that is frequently affected by well-organized LLAP storms (in contrast to locations south of Lake Erie and east of Lake Michigan).

c. *Possible mechanisms for the Tug Hill snowfall maximum*

In this study, we use observations to clarify the mechanisms controlling the inland gradient in lake-effect snowfall from the Ontario shoreline onto Tug Hill. Broadly, we are motivated to better understand these mechanisms, both as a fundamental science question regarding the response of shallow convection to surface forcing, and also to aid in the critical evaluation of conceptual and numerical models used to forecast these high-impact storms. Here, we focus specifically on how convective clouds evolve as they transition onto land and rise over Tug Hill. Our primary observations come from an east–west transect (black dots in Fig. 1b) of four vertically pointing Doppler radars (described in section 2a) that measure vertical profiles of Z_e and Doppler vertical velocity V_R. Below, we present several hypothetical mechanisms to explain the observed inland gradient in lake-effect snowfall. Each of these is shown schematically in Fig. 2. We also briefly note the expected observational signatures associated with each mechanism (summarized in Table 1).

1) Orographic invigoration of convection

Orographic lifting by Tug Hill may invigorate lake-effect convection, increasing updraft speeds and/or cloud depths (Fig. 2a). This could occur if orographic lifting of the inversion layer allows convection to deepen [as illustrated in Lackmann (2011), his Fig. 9.21]. Idealized model simulations support this mechanism for lake-effect snow alongside Lake Erie (Lavoie 1972) and sea-effect snow in Japan (Murakami et al. 1994). Alternatively, orographic invigoration can take place in the absence of any change in inversion height. This occurs over the mountains of the Caribbean island Dominica, where shallow trade wind cumuli are invigorated because of increases in cloud buoyancy associated with layer lifting and because of decreases in buoyancy dilution from entrainment associated with changes in cloud size (Kirshbaum and Smith 2009; Kirshbaum and Grant 2012; Minder et al. 2013). If orographic invigoration is important, then with increasing inland distance from Lake Ontario, profiling radar data should show an increase in echo depth (deepening of convection), an increase in the variability of Z_e and V_R (stronger, more-turbulent updrafts/downdrafts), an increased frequency of $V_R > 0$ (hydrometeor lofting by strong updrafts), and an increase in the upper quartile of Z_e (larger peak convective snowfall intensity).

2) Orographically forced increases in snowfall frequency

Orographic lifting by Tug Hill may increase the frequency or horizontal size of precipitating convective cells (Fig. 2b). If the flow is sufficiently moist and unstable, orographic lifting can trigger new convective cells and precipitation (e.g., Browning et al. 1974; Colle et al. 2008; Smith et al. 2009). Additionally, orographic lifting

[2] At times, both morphologies were observed simultaneously.

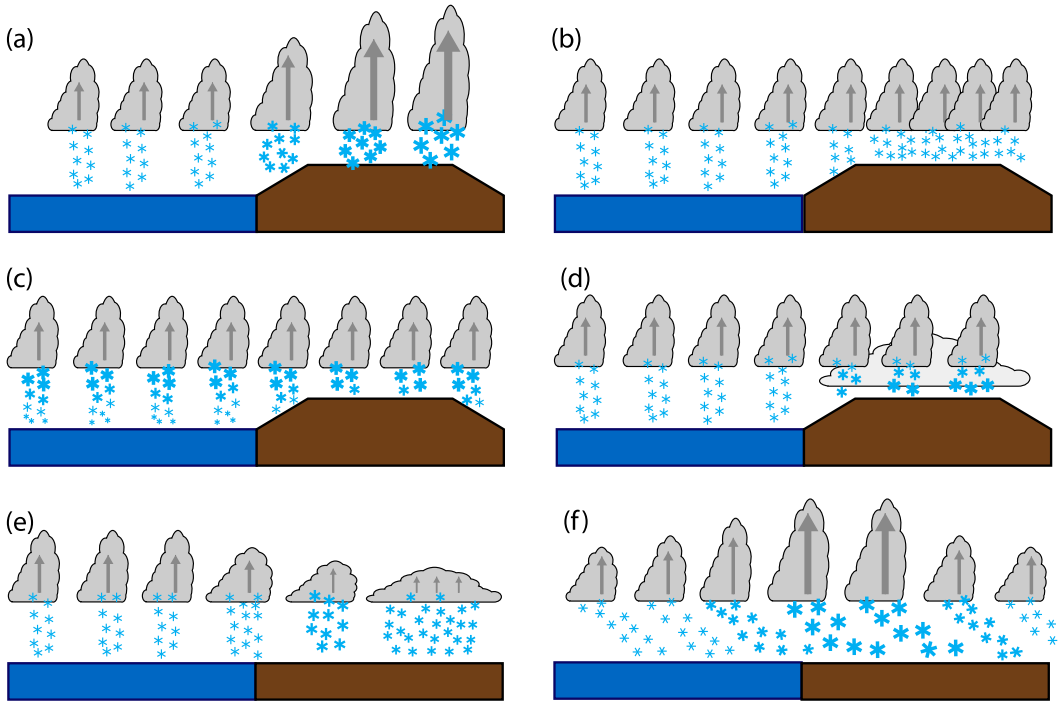

FIG. 2. Hypothetical changes in lake-effect convection and snowfall associated with landfall and orographic forcing. Size of snowflakes represents snowfall rate. Vertical arrows represent updraft speed in clouds. Mean winds are assumed to blow from left to right. Depicted mechanisms include the following: (a) orographic invigoration of convection, (b) orographically forced increases in snowfall frequency, (c) orographic suppression of sublimation, (d) seeder–feeder enhancement, (e) convective-to-stratiform transition, and (f) hydrometeor advection. Elevated terrain is omitted from (e) and (f) to emphasize that these mechanisms do not rely on orographic forcing.

can increase the horizontal scale of clouds (Kirshbaum and Grant 2012). A role for this mechanism is suggested by radar observations collected during the Lake Ontario Winter Storms project that indicated an increase in frequency but not intensity of echoes over Tug Hill relative to upwind locations (Reinking et al. 1993). Furthermore, multiyear statistics show a locally enhanced frequency of radar echoes exceeding 10 dBZ_e over western and upper Tug Hill (Veals and Steenburgh 2015). If this mechanism is important, profiling radar data should show a near-surface echo frequency that increases inland over Tug Hill.

TABLE 1. Predicted profiling radar signatures expected for each of the various snowfall enhancement mechanisms discussed in section 1c.

Mechanism	Predicted profiling radar signature
Orographic invigoration of convection (Fig. 2a)	Echo depth increases with inland distance
	Variability of Z_e, V_R increases with inland distance
	Upper-quartile Z_e increases with inland distance
	Frequency of upward V_R increases with inland distance
Orographic increase in snowfall frequency (Fig. 2b)	Increased echo frequency with inland distance
Orographic suppression of sublimation (Fig. 2c)	$dZ_e/dz > 0$ below cloud base at upwind sites
	dZ_e/dz reduced over Tug Hill relative to upwind
Orographic seeder–feeder enhancement (Fig. 2d)	$dZ_e/dz < 0$ over Tug Hill
	dZ_e/dz more negative over Tug Hill than upwind
Convective–stratiform transition (Fig. 2e)	Increased echo frequency with inland distance
	Variability of Z_e, V_R decreases with inland distance
	Upper-quartile Z_e decreases with inland distance
	Frequency of upward V_R decreases with inland distance
Hydrometeor advection (Fig. 2f)	Uncertain

3) Orographic suppression of sublimation

The orography of Tug Hill may enhance surface snowfall by limiting subcloud sublimation over the terrain relative to upwind locations. Sublimation may be suppressed over Tug Hill by an increase in the relative humidity of subcloud air caused by orographic lifting or by a decrease in the depth of the subcloud layer due to elevated terrain (Fig. 2c). Such orographic effects on sublimation are thought to be important for enhancing sea-effect snow over the mountains of Japan (Murakami et al. 1994) and synoptically generated precipitation over the mountains of Utah (Schultz and Trapp 2003). If orographic suppression of sublimation is important, profiling radar data should indicate a subcloud reduction in snowfall ($dZ_e/dz > 0$ near the surface) at upwind sites that is reduced or eliminated over Tug Hill.

4) Seeder–feeder enhancement

Orographic lifting over Tug Hill may produce shallow stratiform orographic clouds that enhance precipitation because of the seeder–feeder mechanism (Fig. 2d). In this mechanism, seed precipitation generated aloft grows via collection of liquid water as it falls through an orographic feeder cloud (Bergeron 1965). Model simulations suggest that this process is important in the enhancement of sea-effect snow over Japan (Saito et al. 1996; Murakami et al. 1994). In profiling radar data, seeder–feeder enhancement should produce a low-level enhancement of Z_e ($dZ_e/dz < 0$ near the surface) over Tug Hill as a result of growth by collection in orographic clouds that exceeds any similar enhancement over the upwind sites.

5) Convective–stratiform transition

Since landfall of lake-effect convection isolates it from the surface heat and moisture fluxes that sustain it, there should be an inland reduction in the vigor of convective motions. This may produce clouds that have characteristics intermediate between convective and stratiform, analogous to the later stages of the life cycle of deep convection (Yuter and Houze 1995a). These less-convective clouds may be more efficient at producing surface snowfall (Fig. 2e). For instance, a reduction in updraft strength associated with decay of convection could allow snow to fall through a weak updraft to the surface while growing within the moist core of a cloud instead of being lofted by a strong updraft and ejected into dry environmental air where it is more vulnerable to sublimation. Alternatively, increases in cloud width associated with a stratiform transition could increase snowfall frequency. The expected profiling radar signature of a convective–stratiform transition is largely the opposite of the convective invigoration, with the added expectation of increased echo frequency because of wider stratiform echoes.

6) Hydrometeor advection

Horizontal advection of hydrometeors may play an important role in determining the location of the snowfall maximum because of the finite time required for convection to respond to changes in surface fluxes and the finite time required for hydrometeor fallout. For instance, in the time it takes a snowflake falling at $1\,m\,s^{-1}$ to fall 2 km, a $10\,m\,s^{-1}$ horizontal wind could advect it 20 km inland. Accordingly, the location of maximum surface snowfall may be displaced tens of kilometers downwind of the location of maximum surface heat and moisture fluxes or the location of maximum updraft strength (Fig. 2e). Thus, even if convective instability or intensity maximizes near the coast, an inland precipitation maximum may occur. The expected signature of hydrometeor advection in profiling radar data is unclear, since it will depend on the details of hydrometeor trajectories and, in turn, the details of airflow kinematics and hydrometeor terminal fall speeds.

This study uses observations to better constrain the role of the above mechanisms in producing inland variations in snowfall rate. Section 2 describes the profiling radar datasets and other supplementary datasets used. Section 3 presents a case study highlighting the inland transition of lake-effect convection. Section 4 places the observations in a broader context using statistics from 29 separate events. Section 5 provides discussion of how the observations relate to the above-described mechanisms. Section 6 provides a summary and conclusions.

2. Methods

From December 2013 to January 2014 the OWLeS field campaign (http://www.eol.ucar.edu/field_projects/owles) studied lake-effect systems to the east and south of Lake Ontario. This multi-investigator campaign included the deployment of an instrumented aircraft, mobile X-band scanning radars, precipitation and wind profilers, surface observations, and sounding systems (Kristovich 2014). A manuscript describing the field project and its goals is currently in review. Here, we draw on a subset of the OWLeS data to investigate the inland evolution of lake-effect snowfall in the Tug Hill region. All OWLeS-related field observations utilized here were attained from the OWLeS dataset repository maintained by the NCAR Earth Observing Laboratory (EOL) (available online at http://data.eol.ucar.edu/master_list/?project=OWLeS.)

This study utilizes observations collected along an east–west-oriented transect of four sites, stretching from

TABLE 2. Range of dates corresponding to the MRR deployments at each site shown in Fig. 1b. Radars were relocated in late January to conduct an intercomparison; this period is omitted from the table.

Site	Deployment periods
SIB	17 Oct 2013–21 Jan 2014
	29 Jan–19 Mar 2014
SC	6 Nov 2013–20 Jan 2014
NR	18 Oct 2013–28 Jan 2014
	29 Jan–19 Mar 2014
UP	19 Oct 2013–19 Jan 2014

the Lake Ontario shoreline to the upper reaches of Tug Hill (Fig. 1b). The sites, from west to east, include the following: Sandy Island Beach (SIB, 75 m MSL), Sandy Creek (SC, 175 m MSL), north Redfield (385 m MSL), and upper plateau (UP; 530 m MSL). Throughout OWLeS, profiling radar observations were collected at all four sites, while, at two sites (SC and NR), surface meteorology and manual snow observations were also collected. The transect was designed to align with the axis of maximum frequency of lake-effect snowfall and sample the pronounced climatological gradient in snow accumulation that occurs from the shoreline onto Tug Hill (Veals and Steenburgh 2015).

a. *Micro Rain Radars*

At each transect site, a vertically pointing Micro Rain Radar 2 (MRR; manufactured by Metek) was deployed. The MRR is a frequency-modulated continuous-wave Doppler radar with a transmit frequency of 24 GHz (wavelength of 1.24 cm; K-band) and a beamwidth of 2°. Each MRR measured spectral reflectivity at 32 evenly spaced range gates, with a range resolution of 200 m.

The standard processing software provided by Metek is designed for measurement of rain (e.g., Klugmann et al. 1996; Löffler-Mang et al. 1999; Peters et al. 2002). Maahn and Kollias (2012) developed a postprocessing algorithm for the MRR raw data that improves noise removal, velocity dealiasing, and sensitivity. Importantly, this algorithm allows for the collection of high-quality profiles of equivalent radar reflectivity factor Z_e, Doppler radial velocity V_R, and spectral width SW in both rain and snow. We apply the Maahn and Kollias (2012) algorithm to all of our MRR data. Data are also averaged to 60-s time resolution, and data from the first two range gates are discarded as part of the post-processing such that the first usable range gate is centered at 600 m AGL.

The duration of MRR deployment at each site is given in Table 2. Data were collected at all sites from 6 November 2013 to 19 January 2014, a time period that includes nearly all of the OWLeS intensive observing periods (IOPs). Data were collected at SIB and NR over an extended period, allowing for a more robust statistical comparison between these sites. From 25 to 28 January 2014, three of the MRRs were collocated at NR for an intercomparison during a period that included both synoptic and lake-effect snow. The intercomparison revealed only modest (<3 dBZ_e) differences in median Z_e profiles between the radars. We do not attempt any bias correction because of uncertainties associated with the short intercomparison period. As will be shown, these instrumental differences are small compared to the site-to-site differences that are the focus of this study.

b. *X-band profiling radar*

During all or part of four different IOPs, the University of Alabama Huntsville X-Band Profiling Radar (UAH-XPR) was deployed at SC as part of the UAH Mobile Integrated Profiling System (MIPS). The XPR is a vertically pointing Doppler radar with a transmit frequency of 9.410 GHz and a beamwidth of 1.2° (Phillips 2009). Data were collected with a range resolution of 50 m starting at a range of 50 m. A pulse repetition frequency of 1250 Hz was used, and 1-s average data are used for analysis. We discard data from the lowest three range gates to avoid near-field effects. Thus, the XPR provides data at 200-m range and above. As compared to the MRRs, the XPR provides data with higher vertical and temporal resolution, with higher sensitivity, and at lower levels in the atmosphere.

c. *Additional observations*

Surface snow measurements were collected throughout OWLeS at SC and NR. Manual measurements of accumulated snow depth and liquid precipitation equivalent (LPE) were taken at 6-h intervals (0000, 0600, 1200, and 1800 UTC) during IOPs. Measurements were made on 0.61 m $\times$ 0.61 m snow boards that were wiped clean after each measurement. LPE measurements were taken by collecting snow samples using a Snowmetrics coring tube and weighing them. Measurements at NR were made in a clearing surrounded by dense low brush and deciduous trees located 338 m from the MRR deployment, while measurements at SC were taken in a clearing surrounded by dense forest located about 1.8 km from the MRR deployment (Fig. 1b). Additional surface precipitation measurements were made during selected periods by the MIPS at SC. These include accumulated LPE from a hotplate precipitation gauge (Rasmussen et al. 2011) and measurements of hydrometeor size distribution from a Particle Size Velocity (PARSIVEL) optical disdrometer (Löffler-Mang and Joss 2000).

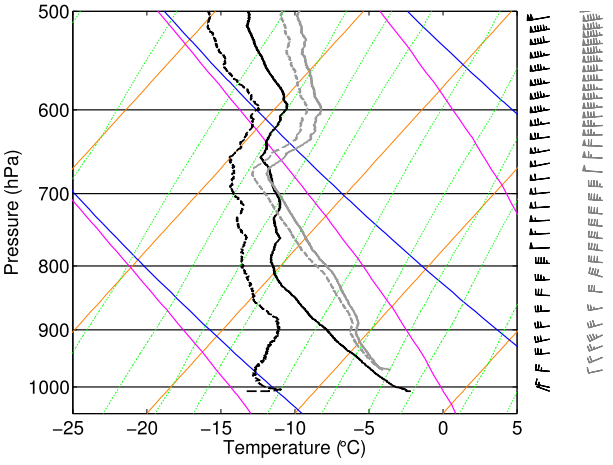

FIG. 3. Skew T–log$p$ plot of a pair of soundings launched during IOP2b on 11 Dec 2013. Solid lines show temperature; dashed lines show dewpoint. Winds are plotted such that a full barb equals 2.5 m s^{-1}. Black lines depict a sounding launched from Darlington, Canada (north shore of Lake Ontario), at 1755 UTC. Gray lines depict a sounding launched from NR at 1727 UTC.

Upper-air observations from radiosondes launched as part of OWLeS are used to provide thermodynamic context. We utilize data from GRAW DFM-09 soundings launched from NR, SC, and the north shore of Lake Ontario at Darlington, Ontario (43.873°N, 78.783°W).

3. Case study of an intense lake-effect storm: IOP2b

a. Overview

Here we focus on an intense lake-effect storm, OWLeS IOP2b, that was oriented along the MRR transect. The event took place primarily on 11 December 2013. During the days surrounding IOP2b, a highly amplified synoptic flow pattern included persistent deep troughing over the Great Lakes region, leading to strong surges of cold arctic air over Lake Ontario. IOP2b took place during one of these surges that began around 0000 UTC 10 December. Heavy lake-effect snowfall commenced over the MRR transect at about 0000 UTC 11 December, following the passage of an upper-level short-wave trough, and continued over the transect until about 0000 UTC 12 December, when convection shifted to the south.

An environmental sounding taken from the north shore of Lake Ontario at Darlington is shown in Fig. 3. This was launched at 1755 UTC 11 December, near the time of heaviest snowfall at SC and NR. It exhibits a dry-adiabatic layer from the surface to about 800 hPa, with moisture well mixed below 900 hPa. Dry near-surface air is present with a dewpoint depression exceeding 10°C. The dry-adiabatic layer is overlain by a moist layer of modest stability extending to about 650 hPa, where it is capped by an isothermal layer. Winds are westerly throughout the profile, with very little directional shear. Considering a representative saturated surface-based parcel with temperature equal to the average of the observed lake temperatures (4°C) and the temperature of the lowest sounding level, the sounding implies a lake-induced CAPE of 1257 J kg^{-1} and an equilibrium level (EL) of 512 hPa. The unidirectional along-lake winds, substantial lake-induced CAPE, and high EL are all typical features associated with strong LLAP band formation in this region (e.g., Niziol et al. 1995).

A sounding launched from within the LLAP band at NR near this time (1727 UTC) is also shown in Fig. 3. It exhibits nearly saturated moist-adiabatic conditions (interrupted by a shallow stable layer at 900 hPa) up to about 675 hPa because of convective transport of air warmed and moistened by surface fluxes over the lake. Saturated conditions near the ground may also be due in part to subcloud sublimation of snowfall. The convective cloud layer is capped by an inversion from about 675 to 600 hPa. The winds are similar in speed and direction in both soundings, down to the 950-hPa level. This suggests that there is minimal orographic flow deflection or deceleration (as might be expected, given the modest topography and weak low-level stratification). Thus, over land there is a strong upslope wind component to facilitate orographic uplift over the western slopes of Tug Hill.

The convective morphology varied over the course of IOP2b. Early in the event (0300–1700 UTC) convection was only loosely organized over the lake, with distinct individual convective elements (e.g., Fig. 4a). During this period, echo coverage and meridional extent increased with inland distance over Tug Hill, suggestive of orographic initiation of new precipitation echoes or an inland increase in echo size. Late in the event (1800–2100 UTC) a pronounced LLAP band structure was observed with a narrow linear organization over both the lake and the land (e.g., Fig. 4b). A map of the frequency of echoes exceeding 10 dBZ_e on 11 December (Fig. 4c) shows that the axis of maximum frequency was oriented along the SIB–SC–NR MRR transect. Along this transect, echo frequency increased from the coastline onto central Tug Hill by about 10%, suggestive of an increase in echo size or number.

According to 6-h manual measurements (Fig. 5), from 0000 UTC 11 December to 0000 UTC 12 December, 6.4 cm of LPE accumulated at NR, and 3.4 cm accumulated at SC. This corresponded with 102.5 cm of accumulated snow depth at NR and 47.8 cm at SC. Thus, as compared to SC, storm-total snowfall at NR was enhanced by a factor of 1.9 for water content and 2.1 for depth. This enhancement was a persistent feature

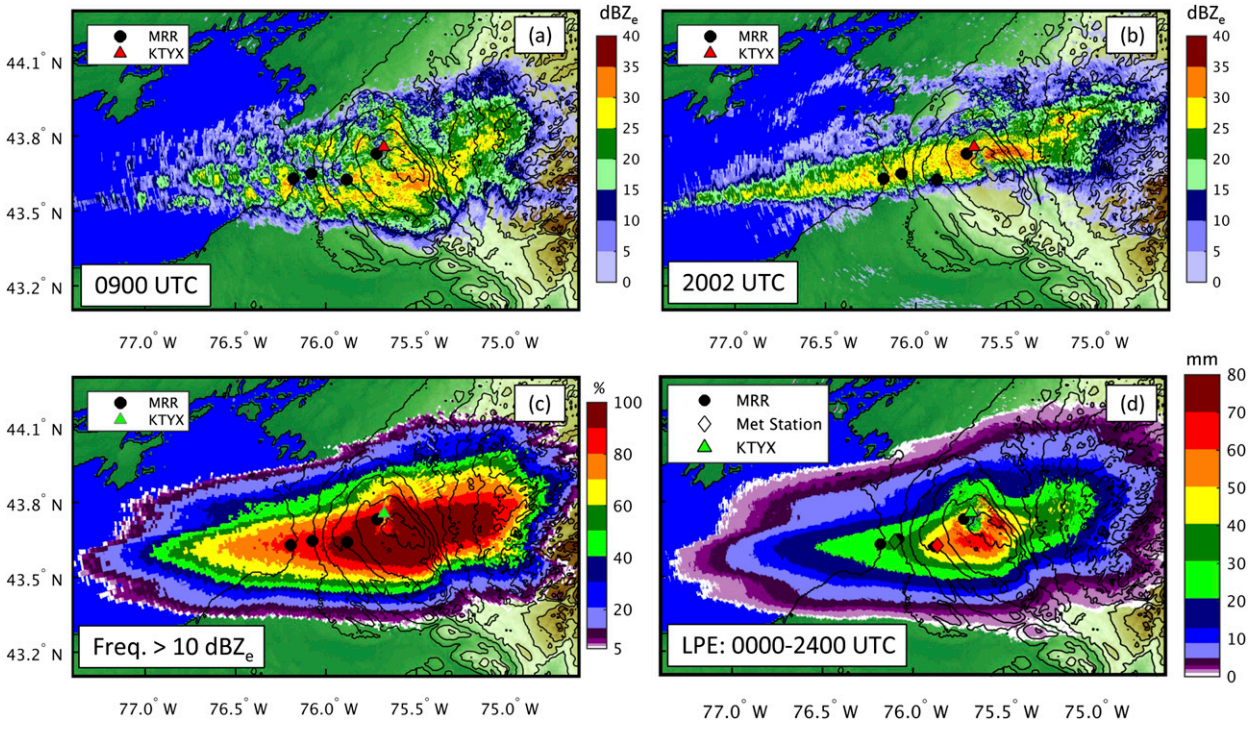

FIG. 4. Measurements from the KTYX WSR-88D during IOP2b (0.5° elevation angle): (a) dBZ_e at 0900 UTC and (b) dBZ_e at 2002 UTC 11 Dec 2013; (c) frequency of KTYX-measured echoes >10 dBZ_e from 0000 UTC 11 Dec to 0000 UTC 12 Dec 2013; and (d) radar-estimated LPE. Note: ground clutter from wind turbines and other sources adversely affects the data to the northeast of the radar.

throughout the duration of the storm: the ratio of 6-h accumulated LPE (depth) at NR to that at SC (Fig. 5) ranged from 1.5 to 3.2 (1.6–3.5). Manual and photographic observations of hydrometeor habits at both SC and NR (not shown) indicated aggregates of dendrites throughout most of the event. However, from 1730 to 2100 UTC, rimed crystals and graupel were frequently observed in the core of the well-organized LLAP band. No systematic differences in crystal habit or degree of riming were observed between the two sites.

Event-total accumulated LPE is estimated from the KTYX WSR-88D, using the database on the Z_e–S relationship $Z_e = 75S^2$, where S is the LPE snowfall rate (in mm h^{-1}) and Z_e is the equivalent radar reflectivity factor. Snowfall rate maps are created from each 0.5° radar sweep and then aggregated to provide 24-h LPE (Fig. 4d). This Z_e–S relationship, typically used for the U.S. Intermountain West (Vasiloff 2002), was chosen for use here because it showed better agreement with surface observations than the standard relation used over the Great Lakes region ($Z_e = 180S^2$). These radar-based estimates show a zonally elongated axis of heavy LPE along the MRR transect and a maximum near the center of Tug Hill. Estimated LPE agrees well with manual surface observations (shaded diamonds in Fig. 4d), reproducing the gradient between SC and NR.

b. MRR observations

The transect of MRR observations characterizes the inland evolution of lake-effect convection. Figure 6 shows time–height plots of Z_e from each of the MRRs during IOP2b. All four sites received nearly continuous snowfall throughout the 24-h period. The deepest

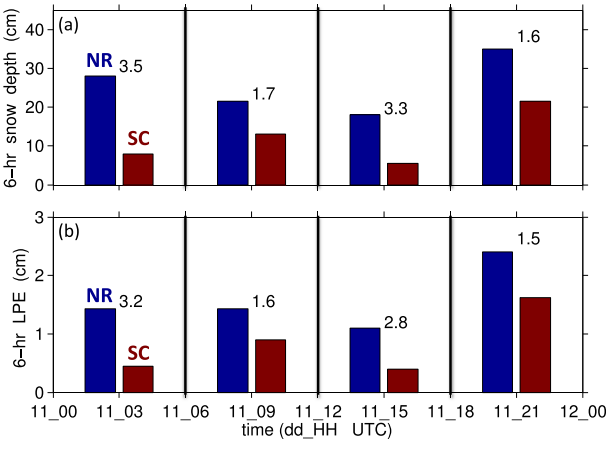

FIG. 5. Manual surface observations of (a) snow depth and (b) LPE at NR and SC. Measurements are collected from boards that are wiped clean at 6-h intervals. The numbers printed over the bars give the ratio between the values at the two sites (NR/SC).

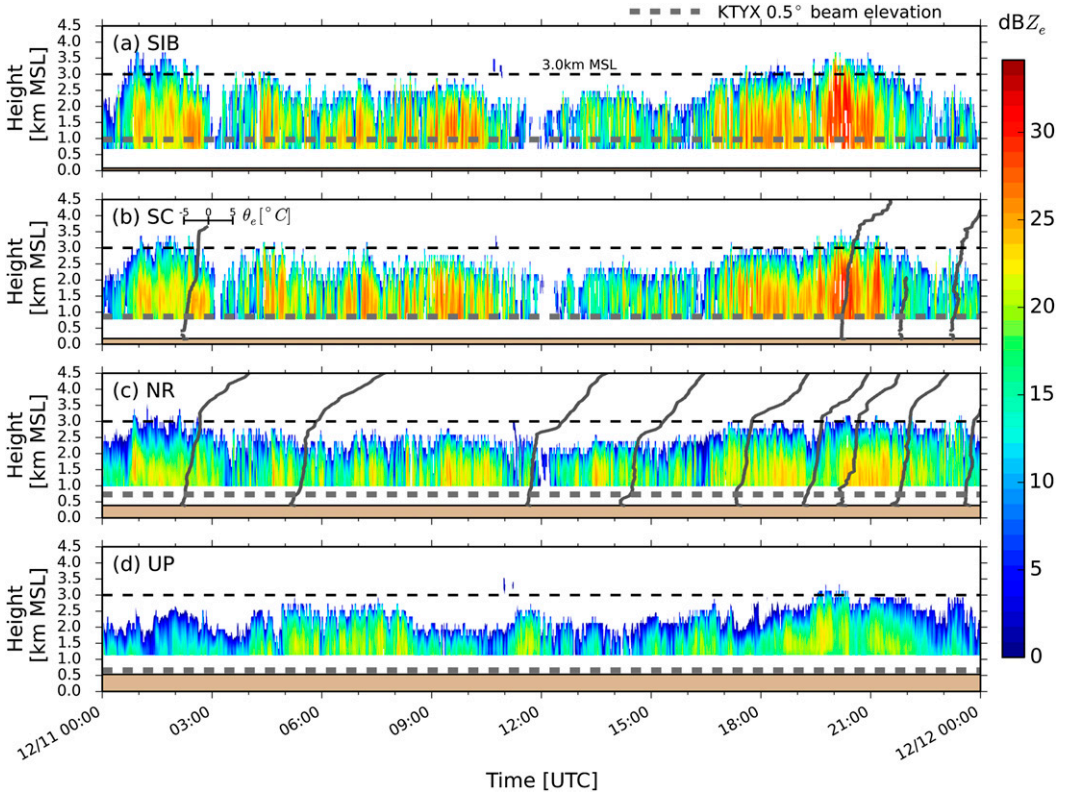

FIG. 6. Time–height plot of MRR equivalent radar reflectivity factor Z_e during IOP2b at (a) SIB, (b) SC, (c) NR, and (d) UP. Solid gray lines in (b)–(c) show profiles of θ_e collected from radiosonde launches at those sites. The thick dashed gray line indicates the approximate height of the center of the KTYX radar beam. The thin dashed black line denotes the 3-km MSL altitude for reference. Below-ground elevations are shaded.

echoes with the highest Z_e occur mostly around 1700–2100 UTC, the same period during which the convection exhibited a narrow LLAP band morphology (Fig. 4b).

Overlain on the time–height plots from SC and NR are profiles of equivalent potential temperature θ_e from soundings launched during the event at these two sites (e.g., Figs. 6b,c). They show that the echoes exist in a layer that is slightly moist stable, as evidenced by the weak vertical gradient of θ_e. The vertical extent of the echoes is constrained by the height of the capping inversion indicated by a strong vertical gradient in θ_e. At SC, the deepest echoes, strongest Z_e, and largest accumulation of LPE and snow depth occur at times with an increased capping inversion height (Figs. 5, 6c).

There is no systematic increase in echo-top height with increasing inland distance. For example, the event-averaged echo top (defined using a threshold of 4.5 dBZ_e) is 300 m lower at NR than SIB, although the difference is not statistically significant at 95% confidence (using a two-tailed Student's t test). Thus, an inland increase in depth of the convection associated with orographic uplift (e.g., Fig. 2a) cannot explain the enhanced snowfall over Tug Hill during IOP2b. The sites near the coast (SIB and SC) show larger Z_e maxima as compared to the sites on the plateau (NR and UP). Additionally, the temporal variability of Z_e is also higher at the coastal sites, consistent with more vigorous convective motions at the coastal locations.

The vertical and temporal structures of Z_e at each site are summarized with contoured frequency by altitude diagrams (CFADs; Yuter and Houze 1995a), which show the frequency distribution of Z_e [per bin size (200 m × 1.5 dBZ_e)] as a function of height (Fig. 7). We normalize all CFAD values by the total number of observation times in the analysis period, giving units of percentage frequency per bin size. Since the normalization (and bin spacing) is constant with height and between sites, CFAD values at different heights and transect locations can be directly compared. Superimposed on the CFADs are the corresponding profiles of median and interquartile range (IQR).

At all four sites the CFAD values generally shift toward higher Z_e with decreasing height, consistent with growth of falling hydrometeors. However, at SIB, SC,

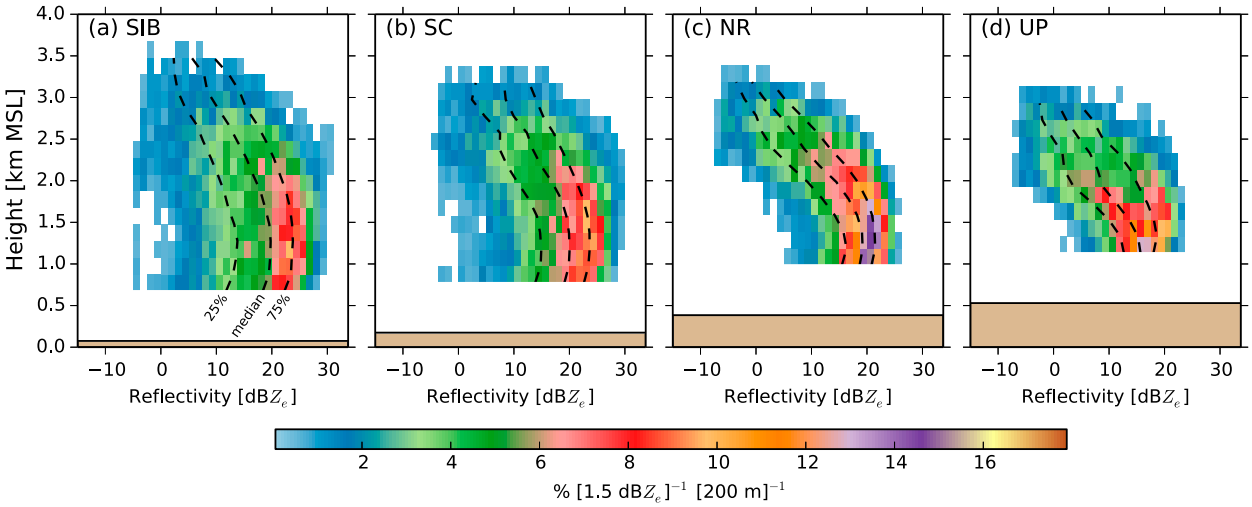

FIG. 7. CFADs of MRR Z_e during IOP2b at (a) SIB, (b) SC, (c) NR, and (d) UP. Dashed lines indicate the median and interquartile range. Below-ground elevations are shaded.

and NR, there is a modest decrease in Z_e below 1 or 1.2 km MSL. Additionally the total frequency of echoes maximizes in the lowest levels. The low-level vertical structure at the upwind sites is notably different than the sites farther inland: at SIB and SC, there is little change in the Z_e distribution with height below about 2 km MSL, whereas at NR and UP, the distribution shifts toward higher Z_e with decreasing height in this layer.

Figure 8 further emphasizes the differences between the coastal and inland CFADs by directly comparing SIB and NR. The median and IQR at the two sites (Fig. 8a) suggests that snowfall intensity is similar at the two sites near the surface (~1 km MSL).[3] However, Z_e increases more rapidly with decreasing height at NR, suggesting either a suppression of snow aloft or an enhancement of snow near the surface. Additionally, the IQR is substantially larger at SIB as compared to NR, a possible signature of more intense convective updrafts and downdrafts at SIB. The total frequency of echoes >5 dBZ_e (Fig. 8b) shows that, above 2.5 km MSL, echoes are less frequent at NR than SIB, consistent with shallower convection. However, below 2 km, echoes are more frequent at NR (present nearly 100% of the time), suggestive of stratiform precipitation processes. The differences between the Z_e distributions at the two sites are further characterized by subtracting the NR and SIB CFADs after interpolating both to a common vertical grid to give a bin-by-bin difference in the frequency of echo occurrence (Fig. 8c). This shows an asymmetric dipole at low levels. Echoes are typically weaker at NR than at SIB, but an increased frequency of echoes weaker than 25 dBZ_e at NR overwhelms the decrease in echoes stronger than 25 dBZ_e such that the total echo frequency at NR is greater (Fig. 8b). This dipole shifts to lower Z_e with increasing height.

Comparing the time–height structure of Doppler radial (vertical) velocities V_R at the four MRR sites also reveals along-band variations (Fig. 9). The sign convention is such that positive (negative) V_R correspond to upward (downward) motions; V_R measures hydrometeor vertical motion (vertical wind speed minus the hydrometeor terminal fall speed). At SIB, V_R is generally downward (-1 to $-1.5\,\mathrm{m\,s^{-1}}$), consistent with falling snow, since terminal fall speeds for snow are typically 0.5–1 $\mathrm{m\,s^{-1}}$. A strong updraft ($V_R > 5\,\mathrm{m\,s^{-1}}$) occurs near 2000 UTC, coincident with one of the deepest observed echoes and the most intense Z_e (Fig. 6a). There is large variability in V_R on short time scales at SIB, consistent with turbulent convective motions. With increasing inland distance, the temporal variability in V_R decreases. Additionally, the frequency of hydrometeor lofting updrafts ($V_R > 0$) increases as convection moves inland from SIB to NR (Fig. 10). These inland variations in V_R are consistent with a decrease in convective vigor and a transition toward stratiform conditions.

The MRR retrievals of Doppler spectral width SW provide a measure of the variability in vertical motion of hydrometeors within an MRR range gate. This variability can be due to turbulent fluctuations in the vertical wind and/or variability in terminal fall speeds of the hydrometeors sampled. Measurements of SW also reveal an

[3] Alternatively, snowfall rates could differ between the sites if particle size, shape, or density varied in such a way to give similar Z_e.

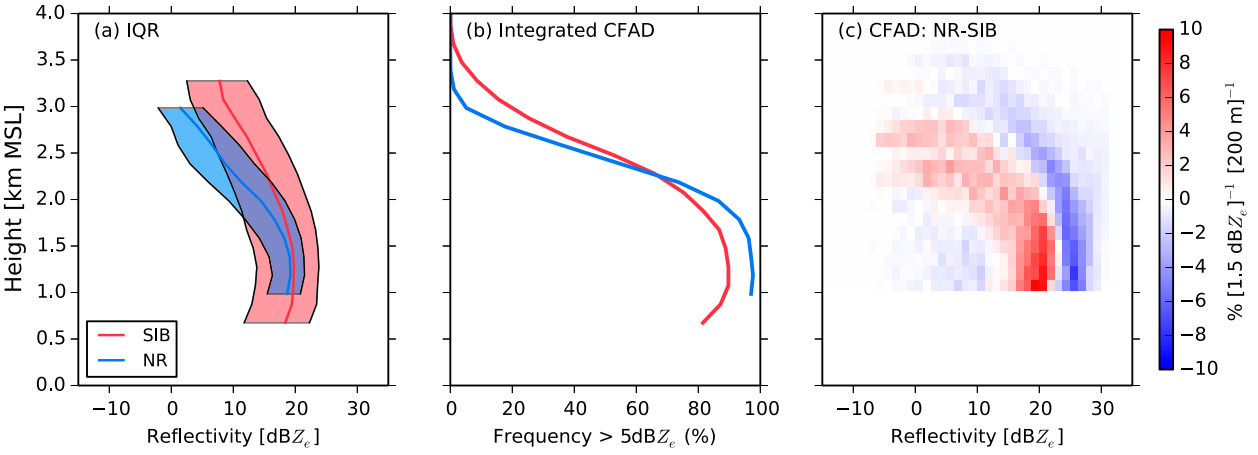

FIG. 8. Comparison of vertical distribution of MRR Z_e during IOP2b at SIB and NR: (a) median and interquartile range, (b) total frequency of >5 dBZ_e, and (c) difference between CFADs (NR − SIB).

inland transition in structure (Fig. 11). At SIB, there are frequently regions of large SW ($>1.5\,\mathrm{m\,s^{-1}}$) throughout the depth of the echo (e.g., at 2000 UTC). These are consistent with turbulent buoyancy-driven convection. Moving inland, the variability of SW decreases, and large values become less common. This is consistent with a weakening of convective motions and a transition toward stratiform conditions. At NR and UP, the largest values of SW are typically found near the surface, suggesting that these variations may be caused in part by mechanically driven turbulence over the rough forested land surface rather than buoyant convection.

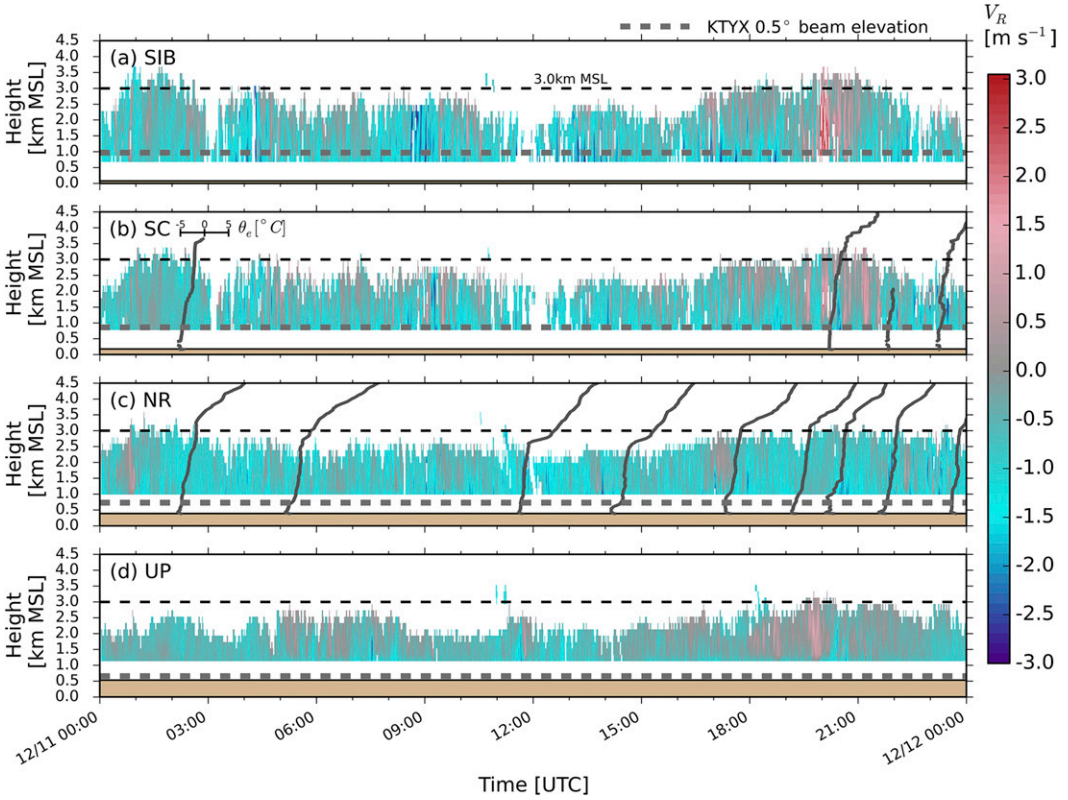

FIG. 9. As in Fig. 6, but for MRR Doppler radial velocity V_R during IOP2b at (a) SIB, (b) SC, (c) NR, and (d) UP.

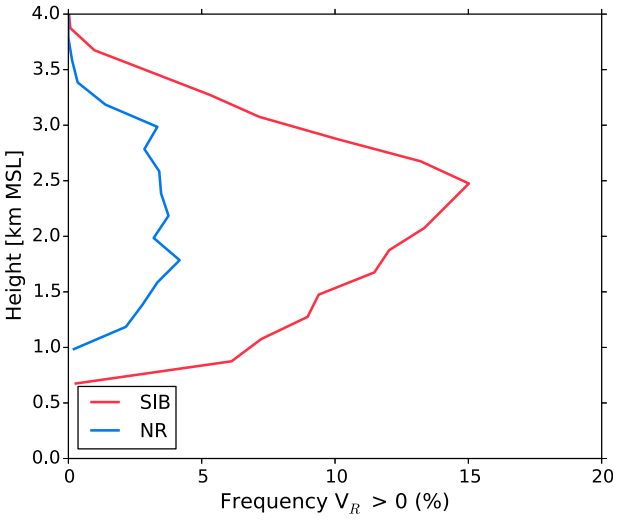

FIG. 10. Frequency of MRR-observed upward hydrometeor motions ($V_R > 0$) during IOP2b. Results are shown for SIB and NR.

c. XPR observations

The MIPS-XPR collected data at SC throughout the duration of IOP2b. These data provide a critical check on the vertical structures inferred from the MRR dataset, since the XPR is a more sensitive radar and operates at a different wavelength. Furthermore, the XPR provides additional details regarding the structure of precipitation because of its much higher vertical and temporal resolution and its ability to record measurements closer to the ground. The time–height structures observed by the XPR (Fig. 12) are broadly similar to the MRR results. At times, the echo tops in the XPR data are more than 500 m higher (Fig. 12a) because of the XPR's superior sensitivity that allows it to sense small ice crystals. The two radars agree well in terms of the depth and timing of the strongest echoes. The radars also generally agree in terms of the magnitude and timing of the strongest V_R (Fig. 12b). The XPR's added detail emphasizes the turbulent nature of the vertical motions.

The XPR's measurements of SW (Fig. 12c) are not directly comparable to the SW measured by the MRR; much of the subpixel variations in vertical motion measured with SW by the MRR are resolved in V_R by the XPR because of its very high temporal resolution and narrower beamwidth. To aid in the comparison, we also calculate the standard deviation of the XPR-measured V_R with a sliding 1-min window $\sigma(V_R)$ to emphasize the resolved high-frequency variability in V_R

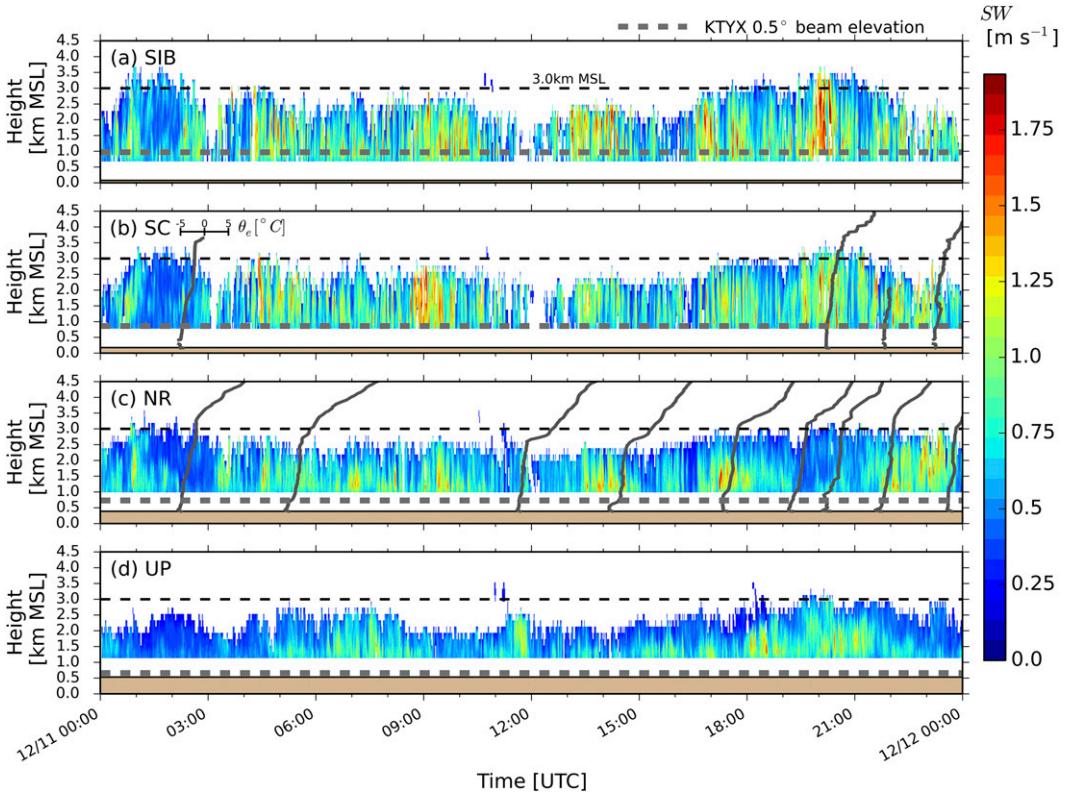

FIG. 11. As in Fig. 6, but for MRR Doppler spectral width SW during IOP2b at (a) SIB, (b) SC, (c) NR, and (d) UP.

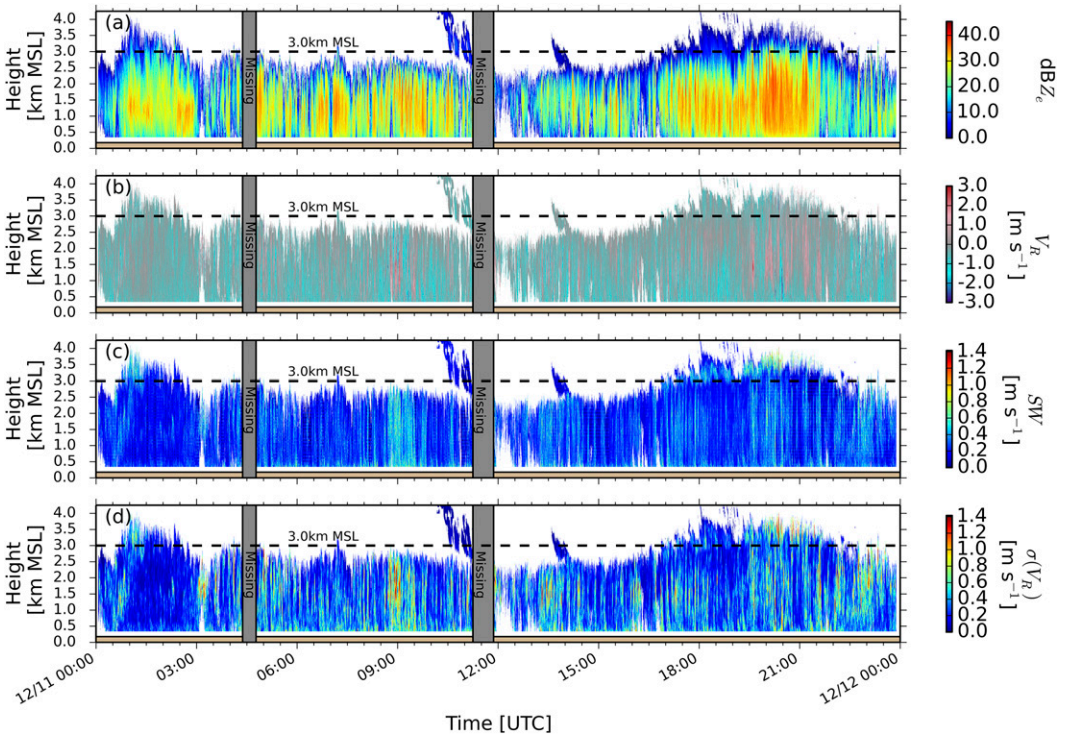

FIG. 12. Time–height plot of XPR observations at SC during IOP2b: (a) Z_e, (b) V_R, (c) SW, and (d) 1-min standard deviation of V_R [$\sigma(V_R)$]. Gray boxes denote periods with missing data.

(Fig. 12d). Both the XPR SW and $\sigma(V_R)$ fields show similar structures to the MRR SW, particularly enhanced values throughout the depth of the echo during strong updrafts.

Figure 13a shows the Z_e CFAD for the XPR data from IOP2b. It shares much of the structure found in the MRR CFAD: minimal variation with height from 0.8 to 1.5 km MSL and decreasing Z_e with height aloft. From

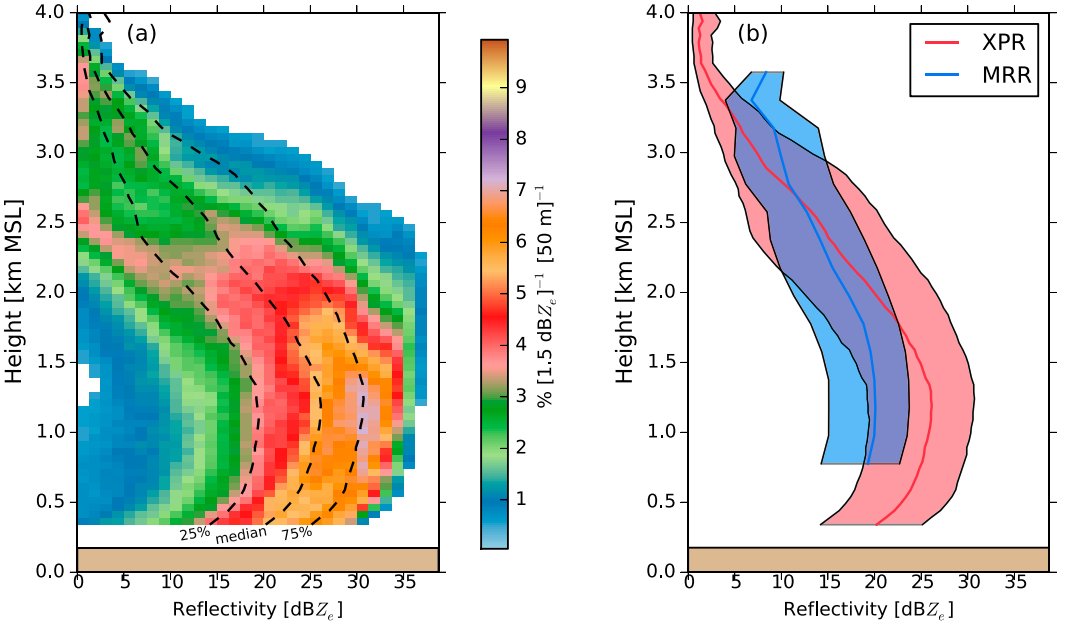

FIG. 13. CFAD of XPR Z_e at SC for IOP2b: (a) XPR CFAD, including median and IQR; and (b) comparison of median and IQR for MRR and XPR CFADs at SC.

about 0.3 to 0.8 km MSL, the XPR retrieves data where the MRR cannot. In this layer, the XPR shows Z_e decreasing toward the surface, with a 5-dBZ_e reduction in the median over the lowest 500 m. This could be an indication of subcloud sublimation of snow beneath cloud base. Alternatively, lofting of hydrometeors by convective updrafts and inland advection may play a role in limiting low-level Z_e and snowfall rates. Snowfall generated aloft over and upwind of SC may be advected downwind over Tug Hill before falling to the surface.

The median and IQR of the XPR and MRR CFADs are compared directly in Fig. 13b. Some important differences are apparent. The XPR Z_e exceeds the MRRs by about 5 dBZ_e from 0.8 to 1.4 km MSL. This difference decreases above this layer and reverses sign at about 2.8 km MSL. Some of this difference may be cause by radar calibration differences or nonuniform filling of the MRR's larger-resolution volume. The differing transmit wavelength λ of the two radars offers another possible explanation. During IOP2b, PARSIVEL optical disdrometer measurements of hydrometeor diameter D were collected at SC by the MIPS. The disdrometer recorded median hydrometeor sizes throughout the event near $D = 1$ mm. This gives approximate size parameters ($x = \pi D/\lambda$) of $x_{\mathrm{XPR}} = 0.10$ and $x_{\mathrm{MRR}} = 0.25$ for the two radars, values near the edge of applicability for Rayleigh scattering theory (e.g., Matrosov 1992). However, during IOP2b, the upper 5th percentile of hydrometeor size often reached or exceeded $D = 5$ mm. These larger particles correspond to $x_{\mathrm{XPR}} = 0.49$ and $x_{\mathrm{MRR}} = 1.3$, sufficiently large for nonnegligible deviations from Rayleigh scattering, particularly for the MRR (e.g., Matrosov 1992). For these particles, more-accurate Mie theory predicts smaller scattering efficiencies relative to Rayleigh theory, with a difference that increases with x up to about $x = 2.2$ (Matrosov 1992). Thus, larger departures from Rayleigh theory for the shorter-wavelength MRR may explain its lower measured values of Z_e relative to the XPR (and KTYX). In this context, the increasing difference between the two radars with decreasing height near the surface could result from a near-surface increase in the numbers of large hydrometeors, as might occur as a result of low-level aggregation.

4. Multistorm statistics

a. MRR observations

To what extent are the observed structures from IOP2b characteristic of other storms? To address this question, we repeat the CFAD analysis for the full selection of lake-effect events observed by the MRRs located at SIB and NR. We focus on these two sites because they were instrumented for the longest duration of the four sites and sample both near-lake and upland conditions. Following Veals and Steenburgh (2015), KTYX data are used to manually identify times with lake-effect snowfall affecting the MRR transect. Some additional times with low echo tops are added based on MRR data. We select events for analysis that have at least 4 h of lake-effect echoes measured by an MRR with gaps of less than 2 h.

The 29 events meeting these criteria and their durations are listed in Table 3. Most of the events correspond to OWLeS IOPs, but several correspond to events that occurred before or after the main OWLeS observing period. A total of 446 h of lake-effect snowfall is included. Of this, 189 h exhibited LLAP band morphology, and 335 h exhibited less-organized broad coverage morphology (many periods exhibited both, as in IOP2b). Event durations ranged from 5 to 39 h (compared with 24 h for IOP2b).

A map of the frequency of echoes >10 dBZ_e over these collected time periods indicates a maximum over the western slopes of Tug Hill centered near NR (Fig. 14). Frequencies increase by over 15% from the Ontario shoreline to NR, suggesting a contribution of increased echo size or frequency to snowfall enhancement. However, some of this inland gradient in echo frequency may be an artifact of overshooting or partial beam filling of the KTYX radar beam, which is centered about 1 km AGL at SIB (Brown et al. 2007). These general structures are similar to those found in IOP2b (Fig. 4c), although the more diverse sampling of storm positions in the multievent analysis leads to a meridional broadening of the frequency contours.

Figure 15 shows profiles of median and IQR of Z_e at SIB and NR for several events selected to show the variety of vertical structures observed. Many of these events share similarities with IOP2b. For instance, in IOPs 1, 3, 5, and 9, the two sites have a very similar median Z_e at 1 km MSL but have different vertical gradients, showing stronger increases in Z_e with decreasing height at NR than SIB. Many events also show a reduced IQR at NR relative to SIB, indicating less temporal variability at the inland site, possibly an indication of an inland reduction of convective activity. Certain events show structures distinct from those of IOP2b (e.g., IOP4, Nov10). Importantly, for all profiles shown, the median and upper quartile of Z_e are never substantially stronger at NR than SIB, despite the much larger mean snowfall at NR. This provides further evidence that increases in the intensity of convection cannot explain the inland enhancement of surface snowfall.

TABLE 3. Lake-effect snow events measured by the MRRs deployed at SIB and NR and used in the bulk CFAD analysis. Start time, end time, and duration is noted for each event.

Event	Start time	End time	Duration (h)
Oct23	0420 UTC 23 Oct 2013	2300 UTC 23 Oct 2013	18.67
Oct24	0320 UTC 24 Oct 2013	0600 UTC 25 Oct 2013	26.67
Oct25	2320 UTC 25 Oct 2013	0600 UTC 26 Oct 2013	6.67
Nov08	0000 UTC 8 Nov 2013	1100 UTC 8 Nov 2013	11.00
Nov10	1104 UTC 10 Nov 2013	2300 UTC 10 Nov 2013	11.93
Nov12	1830 UTC 12 Nov 2013	1000 UTC 13 Nov 2013	15.50
Nov13	1500 UTC 13 Nov 2013	2000 UTC 13 Nov 2013	5.00
Nov18	1700 UTC 18 Nov 2013	0815 UTC 19 Nov 2013	15.25
Nov23	1300 UTC 23 Nov 2013	1200 UTC 24 Nov 2013	23.00
Nov27	1934 UTC 27 Nov 2013	1044 UTC 29 Nov 2013	39.17
IOP1	1200 UTC 7 Dec 2013	1900 UTC 8 Dec 2013	31.00
IOP2b	0000 UTC 11 Dec 2013	0000 UTC 12 Dec 2013	24.00
Dec12	1500 UTC 12 Dec 2013	0100 UTC 13 Dec 2013	10.00
IOP3	0300 UTC 13 Dec 2013	1600 UTC 13 Dec 2013	13.00
IOP4	2300 UTC 15 Dec 2013	0630 UTC 16 Dec 2013	7.50
IOP5	1300 UTC 18 Dec 2013	0300 UTC 19 Dec 2013	14.00
Dec26	2000 UTC 26 Dec 2013	1900 UTC 27 Dec 2013	23.00
IOP7	2100 UTC 6 Jan 2014	2230 UTC 7 Jan 2014	25.50
IOP9	0100 UTC 9 Jan 2014	1900 UTC 9 Jan 2014	18.00
IOP10	1100 UTC 12 Jan 2014	1600 UTC 12 Jan 2014	5.00
IOP13	2200 UTC 18 Jan 2014	0300 UTC 19 Jan 2014	5.00
IOP14	2100 UTC 19 Jan 2014	0200 UTC 20 Jan 2014	5.00
IOP15	0500 UTC 20 Jan 2014	1200 UTC 20 Jan 2014	7.00
IOP22	1630 UTC 27 Jan 2014	1900 UTC 28 Jan 2014	26.50
Jan30	0000 UTC 30 Jan 2014	1200 UTC 30 Jan 2014	12.00
Jan31	1622 UTC 31 Jan 2014	2312 UTC 31 Jan 2014	6.83
Feb06	1750 UTC 6 Feb 2014	1924 UTC 7 Feb 2014	25.57
Feb10	1625 UTC 10 Feb 2014	2359 UTC 10 Feb 2014	7.57
Feb15	0300 UTC 15 Feb 2014	0600 UTC 16 Feb 2014	27.00

As for IOP2b, there is no evidence for an inland increase in the depth of the convection in the multistorm statistics. This holds true for each individual event and the dataset as a whole. For both, the difference in average echo top (threshold of 4.5 dBZ_e) between NR and SIB is not significant at 95% confidence (two-tailed Student's t test).

To isolate structures in the vertical profiles that are common across most events, we create bulk (multievent)

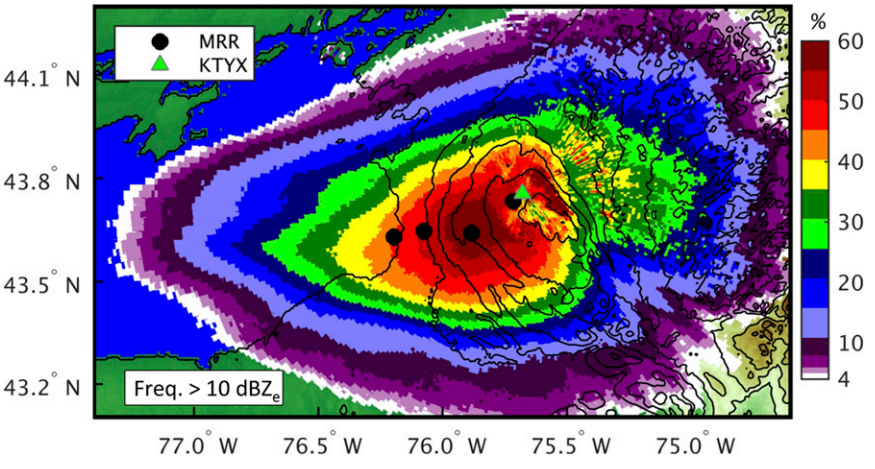

FIG. 14. Frequency of KTYX-measured echoes >10 dBZ_e during events listed in Table 3. Note: ground clutter from wind turbines and other sources adversely affects the data to the northeast of the radar.

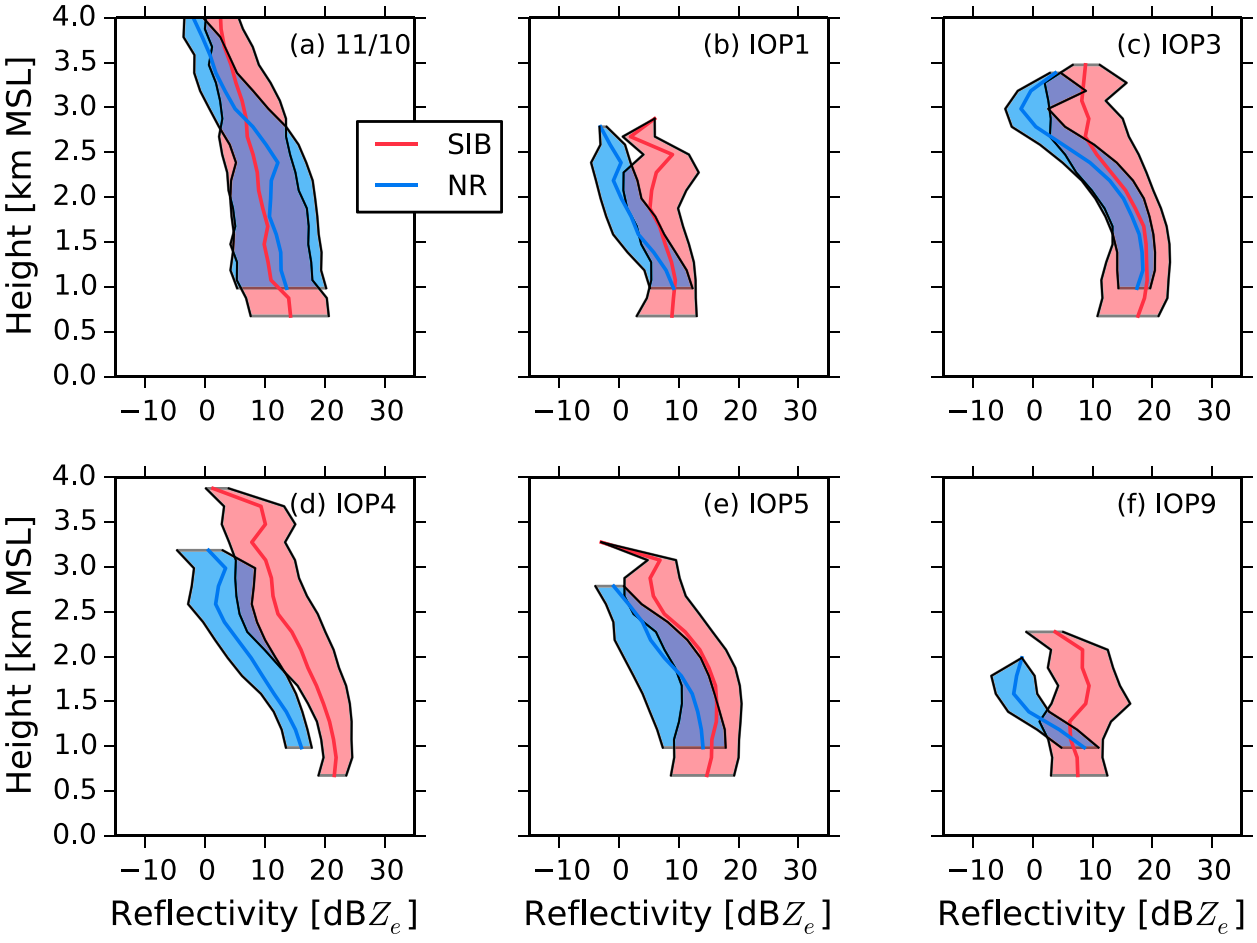

FIG. 15. Median and IQR profiles from SIB and NR (as in Fig. 8a) for select events listed in Table 3.

CFADs, wherein the MRR observations from all 29 events described in Table 3 are combined and compared between SC and NR (Figs. 16, 17). The bulk CFADs share several important similarities with the CFADs from IOP2b. At NR and SIB, there is a general reduction in echo frequency with height above 1.5 km MSL (Fig. 16). The median Z_e at the two sites is similar at 1 km MSL but increases more rapidly with decreasing height at NR (Fig. 17a). As in IOP2b, the difference between the bulk CFADs at SIB and NR shows an asymmetric dipole structure (Fig. 17c). There is a weak reduction in the variability at NR relative to SIB as measured by the IQR (Fig. 17b). The total frequency of echoes >5 dBZ_e is somewhat greater at NR near 1 km, but aloft the frequency is greater at SIB (Fig. 17b). Comparing the frequency of $V_R > 0$ between SIB and NR (Fig. 18) shows that lofting of hydrometeors by updrafts is substantially less common at NR. As for IOP2b, these observations are consistent with an inland convective-to-stratiform transition, with reduced convective variability and shallower more persistent precipitation. There is also a modest decrease in echo frequency below 1 km MSL at SIB (Fig. 17b), possibly indicative of subcloud sublimation or inland advection.

b. *XPR observations*

The XPR was collocated with the MRR at SC for portions of three other LLAP events in addition to IOP2b. Here, we compare MRR and XPR profiles during these periods to explore the generality of the comparison made for IOP2b. Table 4 lists the time periods considered. These periods include portions of IOPs 3, 5, and 7. We focus on times when both radars were operating. For the 7 January event, we separately analyze two periods: a period of light snow from shallow clouds on the southern margin of the LLAP band and a period of intense snow associated with the core of the band. To provide context, for each of these periods two estimates of accumulated LPE are given in Table 4: 1) measurements from the MIPS's hotplate precipitation

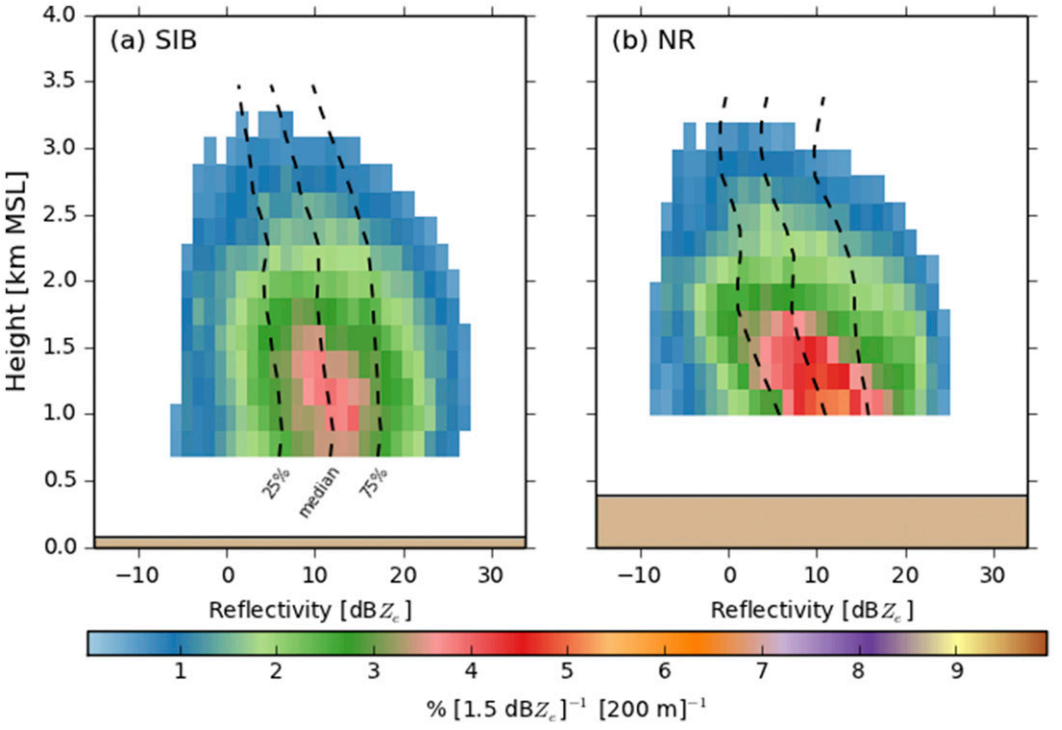

FIG. 16. CFADs of MRR Z_e for data from events listed in Table 3 at (a) SIB and (b) NR.

gauge and 2) manual 6-h measurements from the SC snow-study station.

As in IOP2b, comparing the MRR and XPR profiles for these periods reveals general agreement between the two radars in the overlapping portions of their range (Fig. 19). Both radars show a layer of near-constant Z_e with height starting near 800 m MSL and extending upward to 1–2 km MSL, depending on event. Above this layer, the distribution shifts to higher Z_e with decreasing height. Most profiles show an offset between the two radars, with approximately 2–4-dBZ_e higher values measured by the XPR in the 1–2-km MSL layer. All these periods also show a decrease in XPR Z_e with decreasing height from 800–250 m MSL. In Fig. 19d, this layer of suppressed near-surface dBZ extends to 1 km MSL and is also apparent in the MRR data. As in IOP2b, this low-level suppression of Z_e may relate to subcloud sublimation, hydrometeor lofting, and/or inland advection.

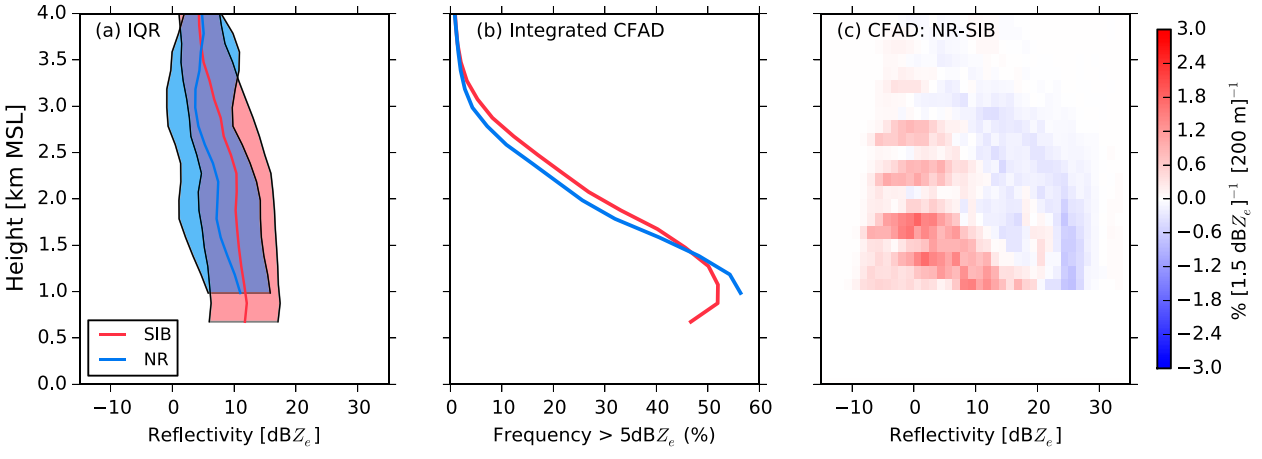

FIG. 17. Comparison of vertical distribution of MRR Z_e during events listed in Table 3 at SIB and NR: (a) median and interquartile range, (b) total frequency of >5 dBZ_e, and (c) difference between CFADs (NR − SIB).

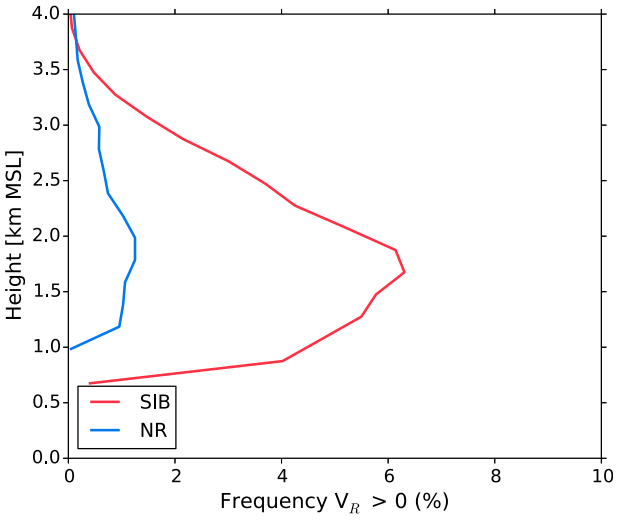

FIG. 18. Frequency of MRR-observed upward hydrometeor motions ($V_R > 0$) during events listed in Table 3. Results are shown for SIB and NR.

5. Discussion

Comparing the above-described case study and multievent statistics with Table 1 helps to narrow the range of potential mechanisms for the Tug Hill snowfall maximum. Most notably, profiling radar observations are inconsistent with the hypothesis of downwind snowfall enhancement because of convective invigoration by orographic lifting (Fig. 2a). With increasing inland distance, our data show (i) no systematic increase in echo depth, (ii) a shift in the reflectivity distribution toward weaker echoes above 1 km MSL, (iii) a decrease in the occurrence of hydrometeor lofting, and (iv) a weakening of turbulent fluctuations. These all point toward an inland decrease in the vigor of convection. The lack of convective invigoration might relate to the modest topography of Tug Hill that only forces weak ascent with minimal impacts on cloud buoyancy or inversion height. Alternatively, vigorous upwind convective cells may effectively remove most of the moist instability form the air before it reaches Tug Hill, limiting the ability of orographic lifting to invigorate convection. In either case, the lack of convective invigoration over Tug Hill may not be representative of lake-effect snowfall enhancement processes over taller mountain ranges (e.g., the Wasatch Mountains) where orographically forced ascent is stronger.

The implications of our observations for other potential mechanisms of snowfall enhancement are more ambiguous. The inland transition of cloud properties may be analogous to the convective-to-stratiform transition that many deep convective clouds undergo (Yuter and Houze 1995b; Houze 1997). In certain settings, stratiform clouds are similarly or more efficient at producing precipitation as compared to convective clouds (Tao and Simpson 1989; Kirshbaum and Smith 2008; Cannon et al. 2012). It is possible that there is a transient phase in the evolution of lake-effect convection as it moves inland and transitions toward stratiform structure when it is more effective at producing heavy snowfall (Fig. 2e). This may be because of increases in echo number/size that enhance snowfall frequency or decreases in hydrometeor lofting that allow snow to fall to the ground within the cloud core, avoiding exposure to the sublimating effects of dry environmental air.

The results do show a modest inland increase in the total frequency of low-level (below 2 km MSL) echoes stronger than 5 dBZ_e (e.g., Figs. 4c, 8b, 14, 17b), consistent with the findings of Veals and Steenburgh (2015). This may be caused by the above-described transition toward stratiform conditions. Alternatively, initiation of new echoes or increases in their horizontal scale could be forced by orographic uplift (Fig. 2b). It is also possible that increased echo frequency is a manifestation of stratiform orographic clouds that enhance snowfall via the seeder–feeder mechanism (Fig. 2d). Increases in Z_e near the surface found in MRR profiles over Tug Hill (but not upwind) also hint at a role for this mechanism. However, the role of such low-level growth is uncertain at best, since Z_e profiles in the lowest 600 m AGL are not available over Tug Hill, and only occasional rimed particles were observed at NR during IOP2b.

Observations at lowland sites indicate a near-surface (below 600 m AGL) suppression of echo frequency and

TABLE 4. Range of times corresponding to the MRR–XPR comparisons shown in Fig. 19. LPE at SC is shown for each time period, as measured by a hotplate gauge and by manual snow-board measurements. Note: the 0600–1200 UTC 7 Jan 2014 manual LPE were affected by strong winds and are thus only a very rough estimate.

Day	Comparison period	LPE (mm; hotplate)	LPE (mm; manual)
12 Dec 2013	2000–2400 UTC	None	Trace
18 Dec 2013	1800–2400 UTC	6	4.61
7 Jan 2014	0000–0600 UTC (band margin)	1.94 (0230 UTC start)	1.0
7 Jan 2014	0600–1200 UTC (band core)	8.31	4.75 (wind affected)

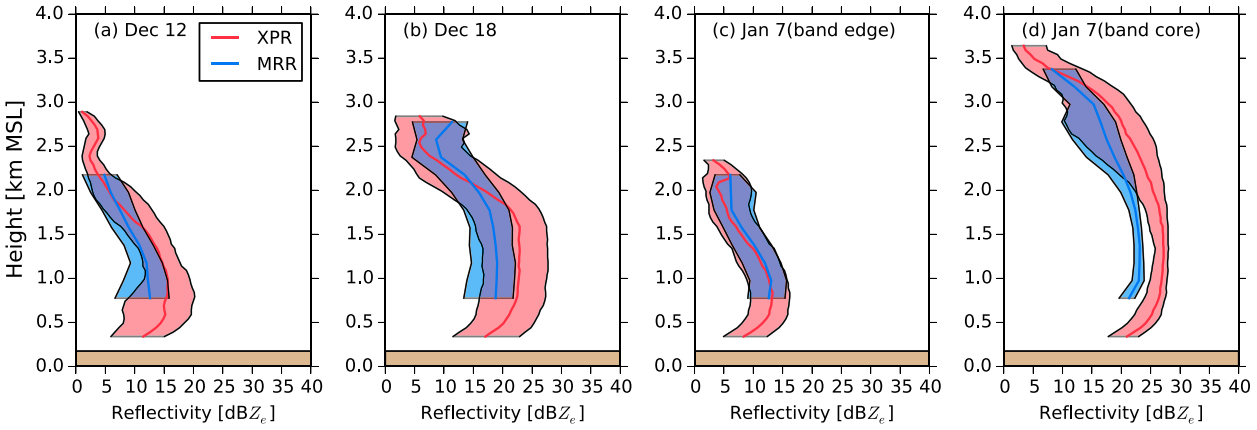

FIG. 19. Comparison of median and IQR of profiles from XPR and MRR at SC (as in Fig. 13b). (a)–(d) Different time periods, as defined in Table 4.

Z_e (Figs. 8b, 13, 17b, 19). These observations are supported by airborne profiling W-band cloud radar data collected by the Wyoming King Air during IOP2b (not shown). This may be a signature of subcloud sublimation reducing snowfall near the coastline and over the lake (Fig. 2c). However, nearly saturated low-level air during snowfall observed by soundings (Fig. 3) and surface observations (not shown) seem to suggest a limited role for sublimation. Still, moist near-surface conditions may, in part, be a result of sublimation. For sublimation to suppress surface snowfall over an extended period, a continued supply of dry air is needed to maintain subsaturated conditions. This may be supplied by lateral influxes into the storm of the low-level dry air seen in environmental soundings (Fig. 3). A more quantitative assessment of the role of sublimation will require detailed analysis of moisture budgets and air parcel trajectories. If sublimation is important at lowland sites, a suppression of sublimation by orographic uplift and reduction in the depth of the subcloud layer may help to explain the relative snowfall enhancement over Tug Hill (Fig. 2c). The lack of low-level Z_e observations at sites on Tug Hill limits our ability to critically test this hypothesis.

Timescales associated with precipitation fallout and the dynamical response to changes in surface fluxes may allow advection to shift the snowfall maximum downwind of the location of maximum surface forcing of convection. This may help explain why snowfall maximizes inland over Tug Hill even though convective forcing is greatest near the shoreline (Fig. 2f). The elevated maximum in Z_e that occurs over upwind locations but not over Tug Hill may be associated with large quantities of snow generated near the coast that descends as it moves inland to reach the ground over Tug Hill. Again, we are limited in our ability to further test this hypothesis in part because of our lack of low-level observations of Z_e over Tug Hill. Further analysis will require detailed consideration of hydrometeor trajectories.

6. Summary and conclusions

A pronounced snowfall maximum exists to the east of Lake Ontario, inland over the 600-m-high Tug Hill Plateau, a region frequently impacted by intense lake-effect snow storms. As lake-effect convection moves inland, it is affected by the transition from water to land and orographic uplift. This study utilized profiling radar observations from the OWLeS field campaign, including an east–west-oriented transect of four K-band Micro Rain Radars, to investigate the inland evolution of lake-effect convection over Tug Hill.

During OWLeS IOP2b, lake-effect convection produced 6.4-cm liquid equivalent snowfall at north Redfield (NR) on the western margin of Tug Hill in a 24-h period. This contrasted with only 3.4 cm just 20 km east at Sandy Creek (SC), closer to the Ontario shoreline. During this event, the KTYX WSR-88D indicated an increase in echo frequency over Tug Hill relative to the shoreline region. MRR observations indicated echoes were confined by a capping inversion near 3.5 km MSL. The equivalent reflectivity factor Z_e in these echoes was strongest below 2 km MSL. X-band profiling radar (XPR) observations collected at SC reproduce a similar time–height vertical structure recorded by the collocated MRR. Data from the XPR indicate a larger Z_e than the MRR below 2 km MSL, potentially because of non-Rayleigh scattering of the MRR beam associated with large snowflakes. Below 600 m MSL, the XPR shows a decrease in Z_e toward the surface.

MRR profiles indicate that the inland enhancement of snowfall totals was not due to orographic invigoration of convection; there was no inland increase in the depth or intensity of lake-effect convection observed. Instead,

with increasing inland distance, echoes become less intense, more uniform, more frequent, less turbulent, and less effective at lofting snow. This evolution is similar to the convective-to-stratiform transition that often occurs with deep convection.

The relative roles of other mechanisms in producing the Tug Hill snowfall maximum remain uncertain. An inland increase in echo frequency appears to contribute to the Tug Hill snowfall enhancement and may be related to orographic initiation of convective or stratiform precipitation. Low-level suppression of Z_e at upwind sites may be a signature of subcloud sublimation or hydrometeor lofting and inland advection.

Multistorm statistics from 29 lake-effect events observed by MRRs at a coastal site (SIB) and at NR demonstrate that the inland weakening of convection, convective-to-stratiform transition, and increase in echo frequency observed during IOP2b are robust features, common to most storms. Four events that include XPR data at SC all indicate a suppression of Z_e beneath about 600 m MSL (a feature also seen at SIB), suggesting that this is also a common feature upwind of Tug Hill.

The data presented here are inconsistent with one hypothetical mechanism that attempts to explain the inland evolution of lake-effect snowfall (orographic invigoration of convection) and provide constraints on others. However, these results do not allow for a complete diagnosis of the relevant mechanisms. Further hypothesis testing will require a more detailed accounting of cloud dynamics and microphysical processes utilizing other datasets collected during OWLeS and numerical modeling experiments.

Acknowledgments. This material is based upon work supported by National Science Foundation Grant 1262090 to the University of Utah and the University at Albany Faculty Research Award Program. We acknowledge the other PIs and participants that contributed to the planning and execution of the OWLeS field campaign. NCAR-EOL maintains the OWLeS data repository. Soundings from Ontario were collected by David Kristovich (University of Illinois), and data from the MIPs was provided by Kevin Knupp (University of Alabama in Huntsville). One of the MRRs was provided by Ronald Smith (Yale). The comparison of MRR and XPR profiles benefited from comments by Bart Geerts and Kevin Knupp. Adam Massmann provided assistance with analysis of sounding and PARSIVEL data. The work also benefited from the helpful comments of three anonymous reviewers and editor Daniel Kirshbaum. We are very grateful to homeowners in the Tug Hill region, the Sandy Creek Central School, and Sandy Island Beach State Park for allowing instrumentation to be deployed on their property. The University of Utah Center for High Performance Computing provided computer support and services. KTYX data was attained from the National Climatic Data Center's archives.

REFERENCES

Alcott, T. I., and W. J. Steenburgh, 2013: Orographic influences on a Great Salt Lake–effect snowstorm. *Mon. Wea. Rev.*, **141**, 2432–2450, doi:10.1175/MWR-D-12-00328.1.

Bergeron, T., 1965: On the low-level redistribution of atmospheric water caused by orography. *Proc. Int. Cloud Physics*, Tokyo, Japan, Amer. Meteor. Soc., 96–100.

Biggerstaff, M., and R. A. Houze Jr., 1991: Kinematic and precipitation structure of the 10–11 June 1985 squall line. *Mon. Wea. Rev.*, **119**, 3034–3065, doi:10.1175/1520-0493(1991)119<3034:KAPSOT>2.0.CO;2.

Brown, R. A., T. A. Niziol, N. R. Donaldson, P. I. Joe, and V. T. Wood, 2007: Improved detection using negative elevation angles for mountaintop WSR-88Ds. Part III: Simulations of shallow convective activity over and around Lake Ontario. *Wea. Forecasting*, **22**, 839–852, doi:10.1175/WAF1019.1.

Browning, K. A., F. F. Hill, and C. W. Pardoe, 1974: Structure and mechanism of precipitation and effect of orography in a wintertime warm sector. *Quart. J. Roy. Meteor. Soc.*, **100**, 309–330, doi:10.1002/qj.49710042505.

Burt, C. C., 2007: *Extreme Weather: A Guide and Record Book.* W. W. Norton & Company, 320 pp.

Cannon, D. J., D. J. Kirshbaum, and S. L. Gray, 2012: Under what conditions does embedded convection enhance orographic precipitation? *Quart. J. Roy. Meteor. Soc.*, **138**, 391–406, doi:10.1002/qj.926.

Colle, B. A., Y. Lin, S. Medina, and B. F. Smull, 2008: Orographic modification of convection and flow kinematics by the Oregon Coast Range and Cascades during IMPROVE-2. *Mon. Wea. Rev.*, **136**, 3894–3916, doi:10.1175/2008MWR2369.1.

Eichenlaub, V. L., and T. W. Hodler, 1979: *Weather and Climate of the Great Lakes Region*. University of Notre Dame Press, 335 pp.

Hartnett, J. J., J. M. Collins, M. A. Baxter, and D. P. Chambers, 2014: Spatiotemporal snowfall trends in central New York. *J. Appl. Meteor. Climatol.*, **53**, 2685–2697, doi:10.1175/JAMC-D-14-0084.1.

Hjelmfelt, M. R., 1990: Numerical study of the influence of environmental conditions on lake-effect snowstorms over Lake Michigan. *Mon. Wea. Rev.*, **118**, 138–150, doi:10.1175/1520-0493(1990)118<0138:NSOTIO>2.0.CO;2.

——, 1992: Orographic effects in simulated lake-effect snowstorms over Lake Michigan. *Mon. Wea. Rev.*, **120**, 373–377, doi:10.1175/1520-0493(1992)120<0373:OEISLE>2.0.CO;2.

——, and R. R. Braham Jr., 1983: Numerical simulation of the airflow over Lake Michigan for a major lake-effect snow event. *Mon. Wea. Rev.*, **111**, 205–219, doi:10.1175/1520-0493(1983)111<0205:NSOTAO>2.0.CO;2.

Holroyd, E. W. I., 1971: Lake-effect cloud bands as seen from weather satellites. *J. Atmos. Sci.*, **28**, 1165–1170, doi:10.1175/1520-0469(1971)028<1165:LECBAS>2.0.CO;2.

Houze, R. A., Jr., 1997: Stratiform precipitation in regions of convection: A meteorological paradox? *Bull. Amer. Meteor. Soc.*, **78**, 2179–2196, doi:10.1175/1520-0477(1997)078<2179:SPIROC>2.0.CO;2.

——, 2014: *Cloud Dynamics.* 2nd ed., International Geophysics Series, Vol. 53, Academic Press, 573 pp.

Kirshbaum, D. J., and R. B. Smith, 2008: Temperature and moist-stability effects on midlatitude orographic precipitation. *Quart. J. Roy. Meteor. Soc.*, **134**, 1183–1199, doi:10.1002/qj.274.

——, and ——, 2009: Orographic precipitation in the tropics: Large-eddy simulations and theory. *J. Atmos. Sci.*, **66**, 2559–2578, doi:10.1175/2009JAS2990.1.

——, and A. Grant, 2012: Invigoration of cumulus cloud fields by mesoscale ascent. *Quart. J. Roy. Meteor. Soc.*, **138**, 2136–2150, doi:10.1002/qj.1954.

Klugmann, D., K. Heinsohn, and H.-J. Kirtzel, 1996: A low cost 24 GHz FM-CW Doppler radar rain profiler. *Contrib. Atmos. Phys.*, **69**, 247–253.

Kristovich, D. A. R., 2014: Tighten your snow belt—New efforts to understand lake-effect storms in the eastern Great Lakes. *16th Conf. on Mountain Meteorology*, Amer. Meteor. Soc., 8.1. [Availible online at: https://ams.confex.com/ams/16MountMet/webprogram/Paper252116.html.]

——, and R. A. Steve, 1995: A satellite study of cloud-band frequencies over the Great Lakes. *J. Appl. Meteor.*, **34**, 2083–2090, doi:10.1175/1520-0450(1995)034<2083:ASSOCB>2.0.CO;2.

Lackmann, G., 2011: *Midlatitude Synoptic Meteorology: Dynamics, Analysis, and Forecasting.* Amer. Meteor. Soc., 360 pp.

Laird, N. F., and D. A. Kristovich, 2004: Comparison of observations with idealized model results for a method to resolve winter lake-effect mesoscale morphology. *Mon. Wea. Rev.*, **132**, 1093–1103, doi:10.1175/1520-0493(2004)132<1093:COOWIM>2.0.CO;2.

——, ——, and J. E. Walsh, 2003a: Idealized model simulations examining the mesoscale structure of winter lake-effect circulations. *Mon. Wea. Rev.*, **131**, 206–221, doi:10.1175/1520-0493(2003)131<0206:IMSETM>2.0.CO;2.

——, J. E. Walsh, and D. A. Kristovich, 2003b: Model simulations examining the relationship of lake-effect morphology to lake shape, wind direction, and wind speed. *Mon. Wea. Rev.*, **131**, 2102–2111, doi:10.1175/1520-0493(2003)131<2102:MSETRO>2.0.CO;2.

Lavoie, R. L., 1972: A mesoscale numerical model of lake-effect storms. *J. Atmos. Sci.*, **29**, 1025–1040, doi:10.1175/1520-0469(1972)029<1025:AMNMOL>2.0.CO;2.

Löffler-Mang, M., and J. Joss, 2000: An optical disdrometer for measuring size and velocity of hydrometeors. *J. Atmos. Oceanic Technol.*, **17**, 130–139, doi:10.1175/1520-0426(2000)017<0130:AODFMS>2.0.CO;2.

——, M. Kunz, and W. Schmid, 1999: On the performance of a low-cost K-band Doppler radar for quantitative rain measurements. *J. Atmos. Oceanic Technol.*, **16**, 379–387, doi:10.1175/1520-0426(1999)016<0379:OTPOAL>2.0.CO;2.

Maahn, M., and P. Kollias, 2012: Improved Micro Rain Radar snow measurements using Doppler spectra post-processing. *Atmos. Meas. Tech. Discuss.*, **5**, 4771–4808, doi:10.5194/amtd-5-4771-2012.

Matrosov, S., 1992: Radar reflectivity in snowfall. *IEEE Trans. Geosci. Remote Sens.*, **30**, 454–461, doi:10.1109/36.142923.

Minder, J. R., R. B. Smith, and A. D. Nugent, 2013: The dynamics of ascent-forced orographic convection in the tropics: Results from Dominica. *J. Atmos. Sci.*, **70**, 4067–4088, doi:10.1175/JAS-D-13-016.1.

Murakami, M., T. Clark, and W. Hall, 1994: Numerical simulations of convective snow clouds over the Sea of Japan: 2-dimensional simulations of mixed-layer development and convective snow cloud formation. *J. Meteor. Soc. Japan*, **72**, 43–62.

Niziol, T. A., W. R. Snyder, and J. S. Waldstreicher, 1995: Winter weather forecasting throughout the eastern United States. Part IV: Lake effect snow. *Wea. Forecasting*, **10**, 61–77, doi:10.1175/1520-0434(1995)010<0061:WWFTTE>2.0.CO;2.

Onton, D. J., and W. J. Steenburgh, 2001: Diagnostic and sensitivity studies of the 7 December 1998 Great Salt Lake–effect snowstorm. *Mon. Wea. Rev.*, **129**, 1318–1338, doi:10.1175/1520-0493(2001)129<1318:DASSOT>2.0.CO;2.

Passarelli, R. E., Jr., and R. R. Braham Jr., 1981: The role of the winter land breeze in the formation of Great Lake snow storms. *Bull. Amer. Meteor. Soc.*, **62**, 482–492, doi:10.1175/1520-0477(1981)062<0482:TROTWL>2.0.CO;2.

Peace, R., Jr., and R. Sykes Jr., 1966: Mesoscale study of a lake effect snow storm. *Mon. Wea. Rev.*, **94**, 495–507, doi:10.1175/1520-0493(1966)094<0495:MSOALE>2.3.CO;2.

Peters, G., B. Fischer, and T. Andersson, 2002: Rain observations with a vertically looking Micro Rain Radar (MRR). *Boreal Environ. Res.*, **7**, 353–362.

Phillips, D. W., 2009: UAHuntsville X-Band Profiling Radar (XPR). *34th Conf. on Radar Meteorology*, Williamsburg, VA, Amer. Meteor. Soc., 11.7. [Available online at https://ams.confex.com/ams/34Radar/techprogram/paper_155613.htm.]

Rasmussen, R. M., J. Hallett, R. Purcell, S. D. Landolt, and J. Cole, 2011: The hotplate precipitation gauge. *J. Atmos. Oceanic Technol.*, **28**, 148–164, doi:10.1175/2010JTECHA1375.1.

Reinking, R. F., and Coauthors, 1993: The Lake Ontario Winter Storms (LOWS) project. *Bull. Amer. Meteor. Soc.*, **74**, 1828–1828, doi:10.1175/1520-0477-74-10-1828.

Saito, K., M. Murakami, T. Matsuo, and H. Mizuno, 1996: Sensitivity experiments on the orographic snowfall over the mountainous region of northern Japan. *J. Meteor. Soc. Japan*, **74**, 797–813.

Schultz, D. M., and R. J. Trapp, 2003: Nonclassical cold-frontal structure caused by dry subcloud air in northern Utah during the Intermountain Precipitation Experiment (IPEX). *Mon. Wea. Rev.*, **131**, 2222–2246, doi:10.1175/1520-0493(2003)131<2222:NCSCBD>2.0.CO;2.

Smith, R. B., P. Schafer, D. J. Kirshbaum, and E. Regina, 2009: Orographic precipitation in the tropics: Experiments in Dominica. *J. Atmos. Sci.*, **66**, 1698–1716, doi:10.1175/2008JAS2920.1.

Steiger, S. M., and Coauthors, 2013: Circulations, bounded weak echo regions, and horizontal vortices observed within long-lake-axis-parallel–lake-effect storms by the Doppler on Wheels. *Mon. Wea. Rev.*, **141**, 2821–2840, doi:10.1175/MWR-D-12-00226.1.

Tao, W.-K., and J. Simpson, 1989: Modeling study of a tropical squall-type convective line. *J. Atmos. Sci.*, **46**, 177–202, doi:10.1175/1520-0469(1989)046<0177:MSOATS>2.0.CO;2.

Vasiloff, S., 2002: Investigation of a WSR-88D Z-R relation for snowfall in northern Utah. *Extended Abstracts, 16th Conf. on Hydrology*, Orlando, FL, Amer. Meteor. Soc., 3.18. [Available online at https://ams.confex.com/ams/annual2002/webprogram/Paper26411.html.]

Veals, P. G., and W. J. Steenburgh, 2015: Climatological characteristics and orographic enhancement of lake-effect precipitation east of Lake Ontario and over the Tug Hill Plateau. *Mon. Wea. Rev.*, **143**, 3591–3609, doi:10.1175/MWR-D-15-0009.1.

Yuter, S. E., and R. A. Houze Jr., 1995a: Three-dimensional kinematic and microphysical evolution of Florida cumulonimbus. Part II: Frequency distributions of vertical velocity, reflectivity, and differential reflectivity. *Mon. Wea. Rev.*, **123**, 1941–1963, doi:10.1175/1520-0493(1995)123<1941:TDKAME>2.0.CO;2.

——, and R. A. Houze, Jr., 1995b: Three-dimensional kinematic and microphysical evolution of Florida cumulonimbus. Part III: Vertical mass transport, mass divergence, and synthesis. *Mon. Wea. Rev.*, **123**, 1964–1983, doi:10.1175/1520-0493(1995)123<1964:TDKAME>2.0.CO;2.